Final Report (8/1/04-7/31/07) ARO YI Project: Development of Micromachined TWT/BWOs Operating Above 100 GHz

There is an increased interest for systems operating above 100 GHz due to a variety of applications including radio astronomy, detection of chemical and biological agents, and imaging for medical and security purposes. In this project we investigated applying deep reactive ion etching (Deep RIE) and laser silicon micromachining techniques for developing low cost high frequency THz systems (f>100 GHz).

During the reporting period, the research effort focused mainly on the analysis of passive micromachined waveguide structures and integrated sources that can be used as building elements for Traveling Wave Tubes (TWTs) operating above 100 GHz. This effort was also complemented by an NSF supported effort on THz micromachined structures. More specifically the following topics were investigated:

1) Theoretical analysis and *first ever* experimental study of silicon micromachined and metal waveguide pieces around 400 GHz.
2) Development of silicon micromachined 3-pole filter at 400 GHz.
3) Analysis of Optimal Cut in “Split-Block” Micromachined Waveguides.
4) Analysis of Meander Micromachined Waveguides in W-Band and 400 GHz.
5) Analysis of Meander Micromachined Waveguides and Transitions in W-Band.
6) Development of first-ever silicon micromachined THz multiplier.
7) Development of power combining THz multiplier.

The following sections describe in more detail the various findings for all the previously mentioned research items.

1. Analysis and Characterization of Micromachined and Metallic Waveguides at 400 GHz.

Several straight waveguide pieces were designed to operate around 400 GHz. The pieces were built using deep reactive ion etching and laser silicon micromachining techniques in a “split-block” configuration. The latter means that the structure is divided in half along a symmetry plane and two identical halves are fabricated at the same time. The two halves are then bonded together with various techniques. For our initial investigation, we decided to split the waveguide in the H-plane (i.e. horizontally) and also fabricate a re-usable test fixture and package that can host the micromachined components with high alignment accuracy and interface with the ABmm network analyzer available at JPL for 400 GHz measurements. A photo of some of the fabricated straight waveguide pieces is shown in Fig. 1 (each piece is 11.81 mm long). A 400 GHz metallic waveguide which is a replica of a “split block” micromachined waveguide was also fabricated and tested to verify the accuracy of our approach. Measured results for 400 GHz micromachined components were reported for the first time ever and a journal paper was submitted to the *IEEE Microwave and Wireless Components Letters*.

A schematic of the test fixture that was used for the “split-block” assembly and THz measurements is shown in Fig. 2. The two pieces were placed in the brass fixture, which will both hold the individual pieces in place as well as sandwich them together to form

the waveguide. Some concern about leakage into the package was examined. It was found the metalizing the interface between the silicon waveguide face and the measurement waveguide face significantly reduced the leakage. From this we concluded that coating the entire piece with gold is the best approach to develop low-loss micromachined waveguide components. Photos of the actual brass fixture are shown in Figs. 3-4, along with a close-up of the assembled waveguide opening. Figure 5 shows a photo of the actual THz measurement set-up assembled at JPL.

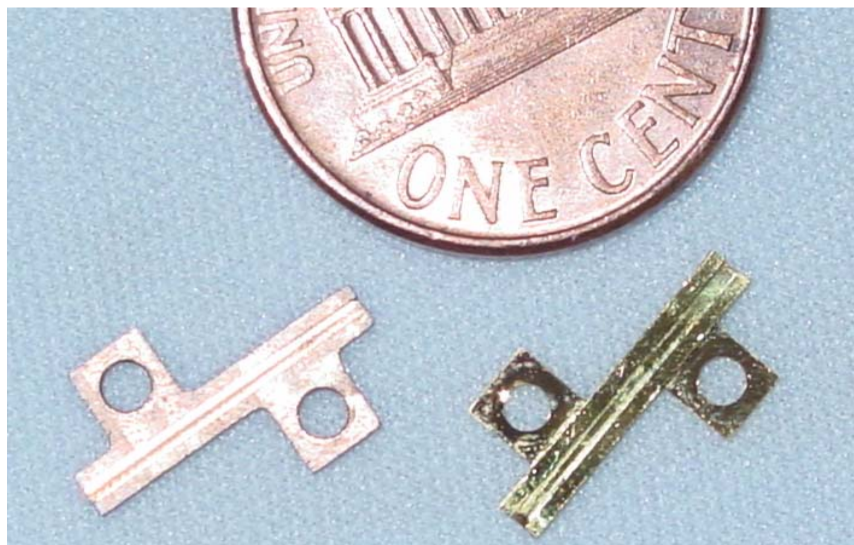

Fig. 1 Photo of silicon micromachined waveguide pieces for 400 GHz operation. The two big holes are used for alignment purposes.

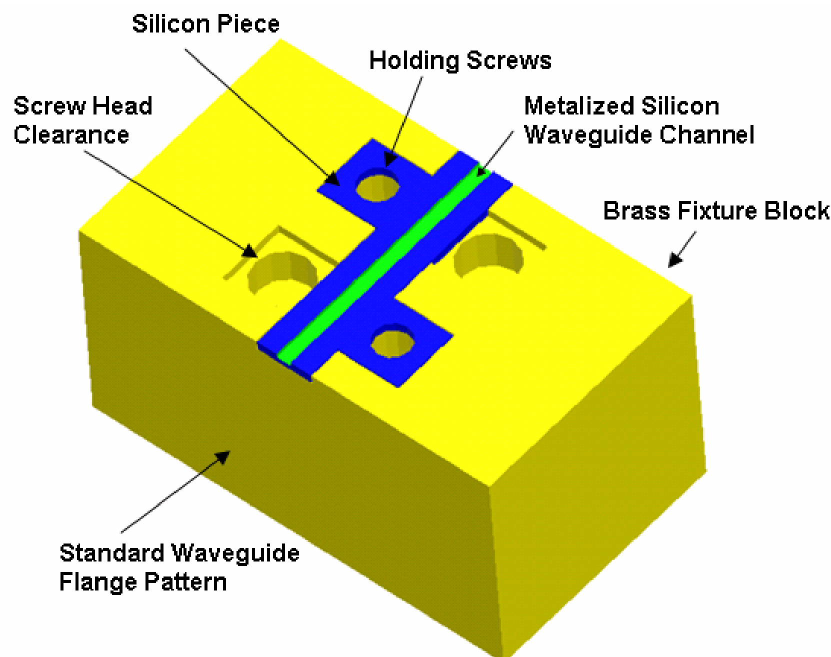

Fig. 2 Schematic of the test fixture for the measurement of the “split-block” micromachined components.

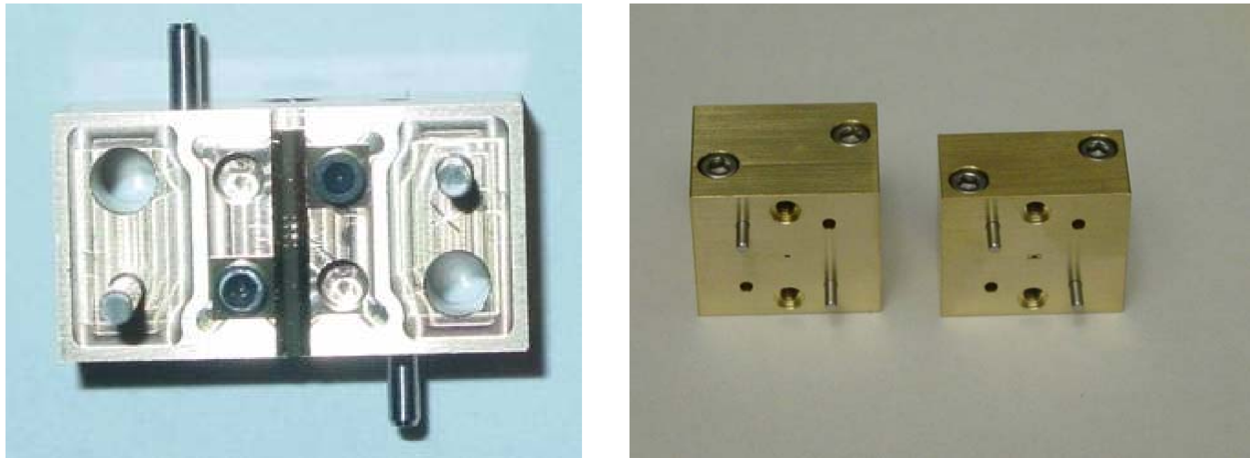

(a) (b)

Fig. 3 a) Top view of half of the brass fixture and b) assembled brass fixtures for 400 GHz measurements.

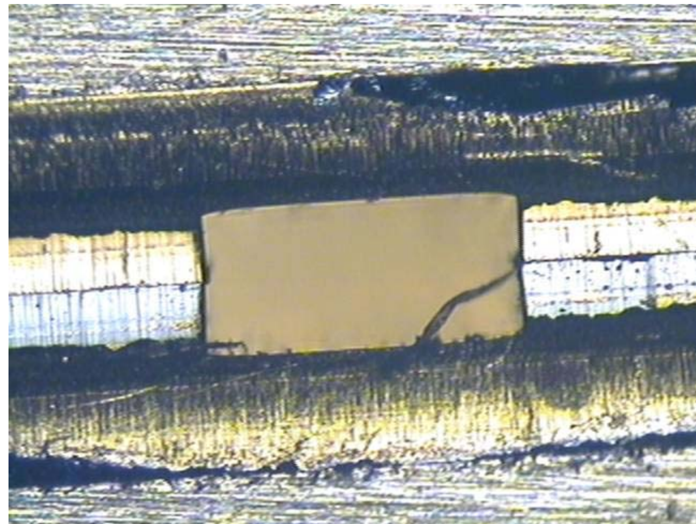

Fig. 4 Close-up photo of the waveguide opening of an assembled micromachined waveguide.

Measured results for the silicon micromachined straight waveguide piece are shown in Fig. 6. A photo of the metallic waveguide and associated measurements are shown in Figs. 7-8. In order to draw a good conclusion from the data, we elected to curve fit the data using a 3rd order polynomial. From Fig. 6 one can see that loss is very low from 350 to 460 GHz (avg. ~ 0.086 dB/mm), and compares well with that of the metallic waveguide. **This is the first ever reported experimental result for a silicon micromachined waveguide at 400 GHz**. The larger loss of the silicon waveguide could be attributed to a few possible causes. The slight slope of the silicon waveguide causes an improper interface with the measurement system, creating small gaps for energy to leak out, something not present on the metal insert. The split in the H-Plane could also cause some additional losses, but we intend to examine the extent of that contribution with an

E-Plane fabrication. Lastly, the condition of the surfaces can contribute to loss. We performed an optical profilometer analysis on the broad surface and determined the surfaces to be comparable, with the silicon guide actually having a more uniform flat surface. At this point we are investigating the sources of increased loss for the silicon waveguide. We are especially looking into the way we split the waveguide (see section 3 for more details), as well as metal coverage issues.

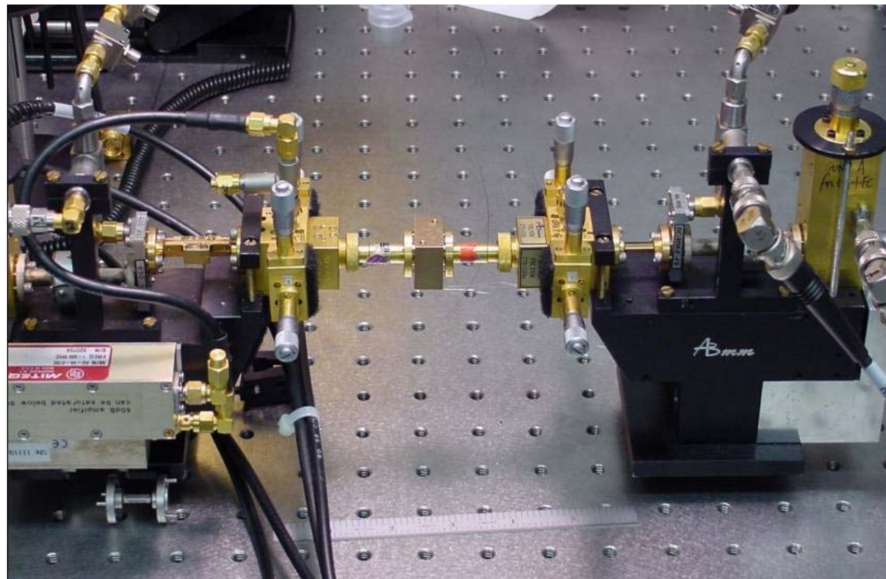

Fig. 5 Photo of the THz measurement system assembled at JPL.

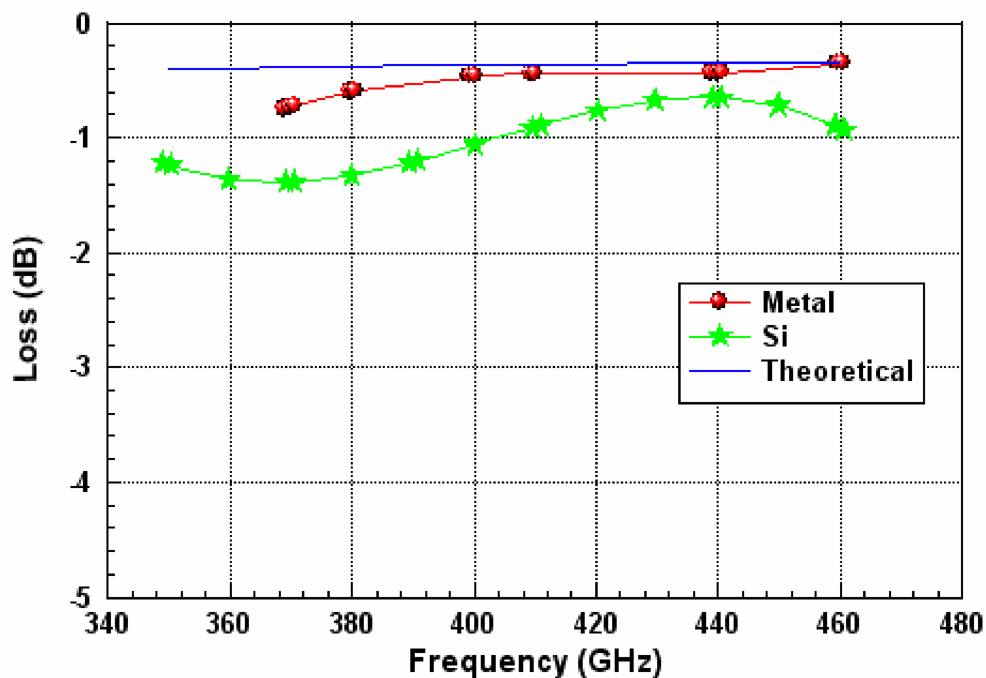

Fig. 6 Measured transmission of straight piece of micromachined waveguide. A comparison is made with the metallic piece and with theory.

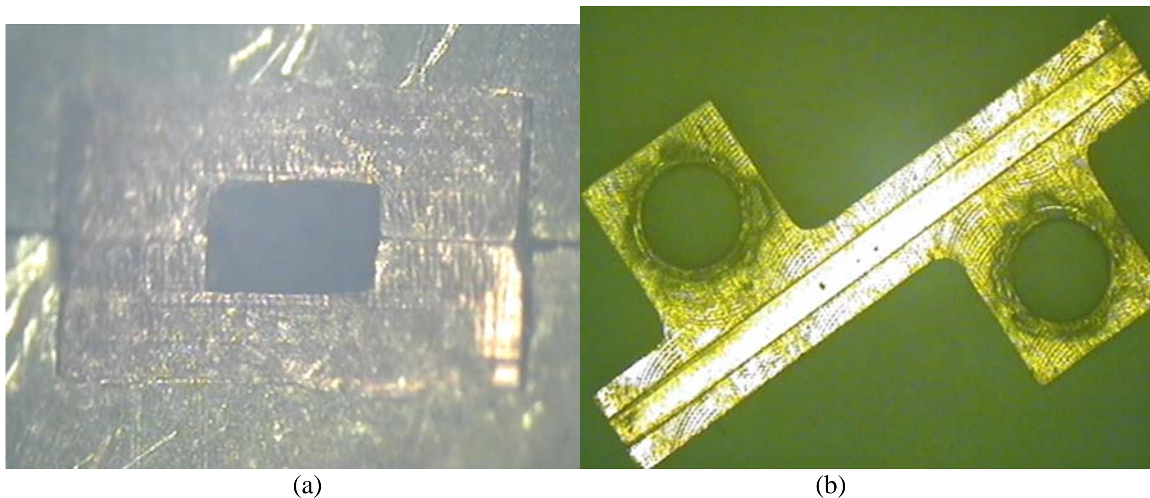

(a) (b)

Fig. 7 a) Close-up of the metallic waveguide opening and b) top view of the metallic waveguide. The waveguide is a replica of the silicon micromachined waveguide.

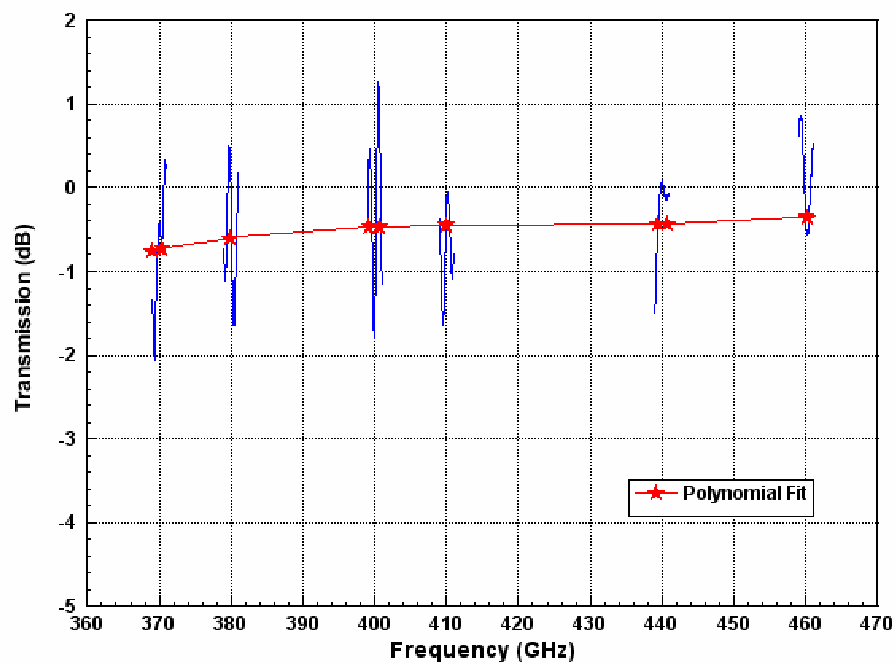

Fig. 8 Measured results for the metallic waveguide.

2. Analysis and Characterization of Micromachined 3-Pole Filter at 400 GHz.

It was decided to pursue a filter design in the area of 400 GHz to insure both an advancement in frequency range using silicon and a relatively large waveguide to handle as a first run. For this frequency range, WR-2.5 sized waveguide is the most suitable (295-446 GHz). It should be noted this is not a standard sized waveguide as standard

sizes do not exist below WR-3. With this in mind the inside dimension of the waveguide were set at 25 by 12.5 mils.

A design for the filter already existed at 600 GHz and just needed to be scaled and optimized for the 400 GHz range. The design is a 3-cavity filter utilizing inductive irises as shown in Figure 9.

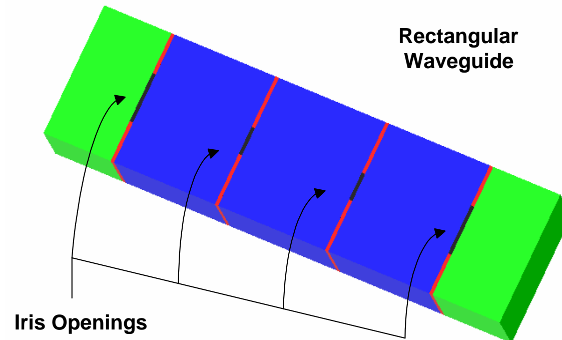

Fig. 9 Top view of the waveguide filter layout.

A 5% bandwidth for the filter centered at 400 GHz was optimized using HFSS and Optimetrics. Two different simulations were done with the changing factor being found in the thickness of the iris walls and their taper. The first simulation included iris wall thicknesses of 10 µm with a total taper of 2 µm from top to bottom and the second simulation included iris wall thicknesses of 20 µm with a total taper of 5 µm from top to bottom (see Figs. 10-11). A more detailed analysis of the taper effect on the filter performance is presented at the end of this section.

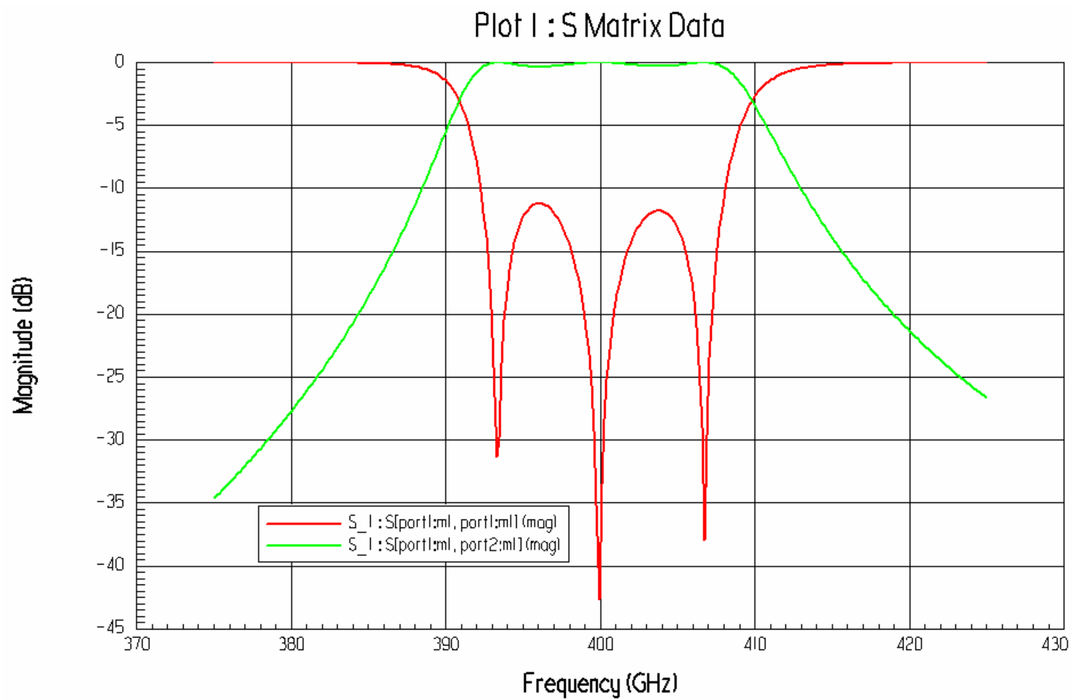

Fig. 10 Simulation results of 5% BW filter with 10 µm thick walls and 2 µm taper.

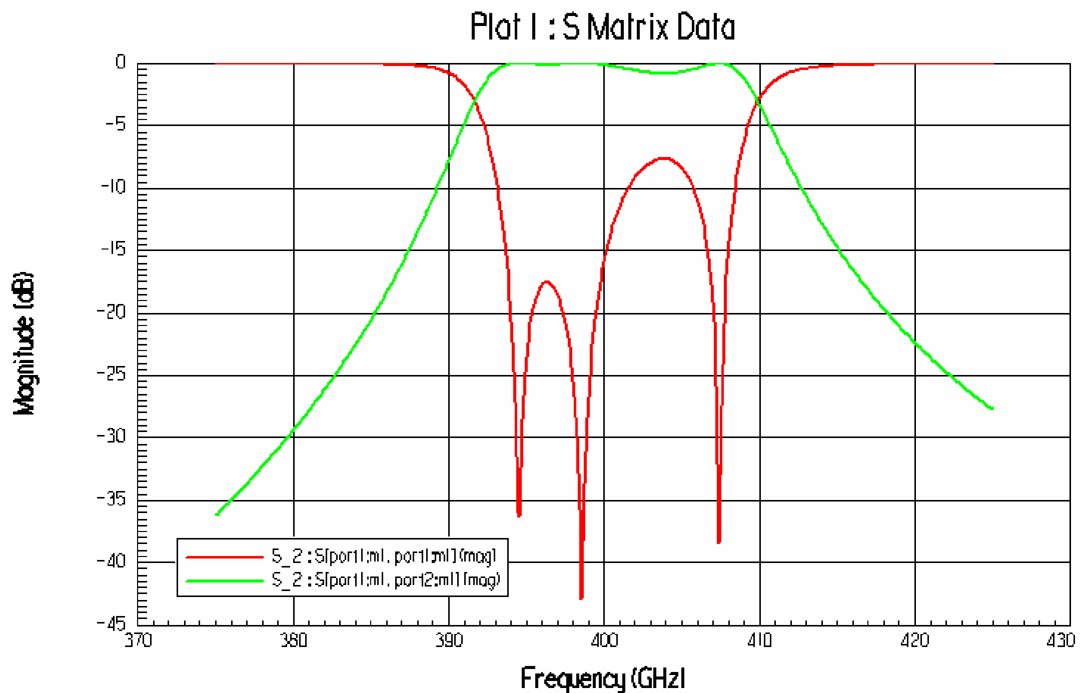

Fig. 11 Simulation results of 5% BW filter with 10 µm thick walls with a taper change to 5 µm.

Photos of the fabricated micromachined filters using deep RIE are shown in Figs. 12-13.

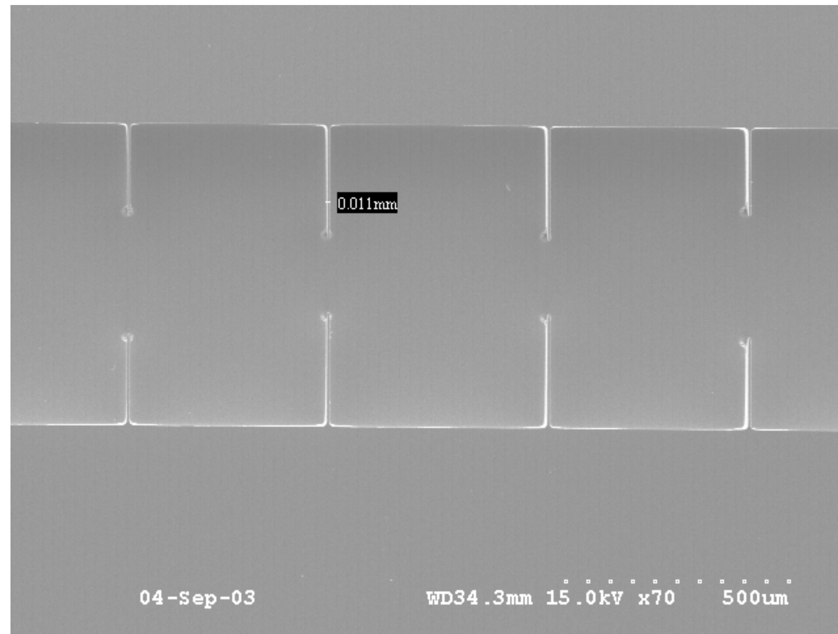

Fig. 12 SEM of the micromachined cavity filter with the 10 µm wide iris walls.

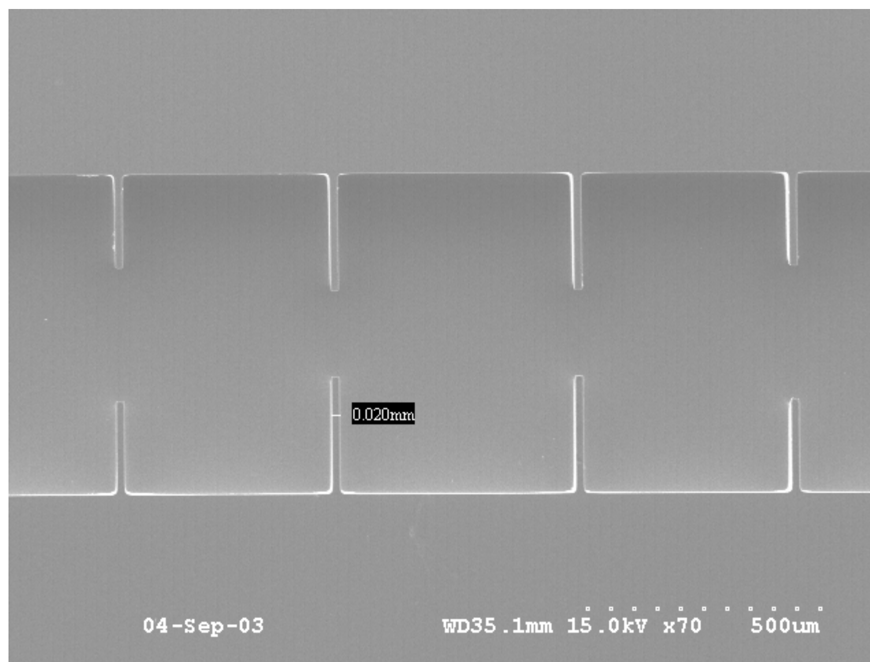

Fig. 13 SEM of the micromachined cavity filter with the 20 µm wide iris walls.

Measured results of the filter are shown in Fig. 14, where it can be observed that the filter exhibits a loss of around 7-8 dB. The reasons for this are currently being investigated.

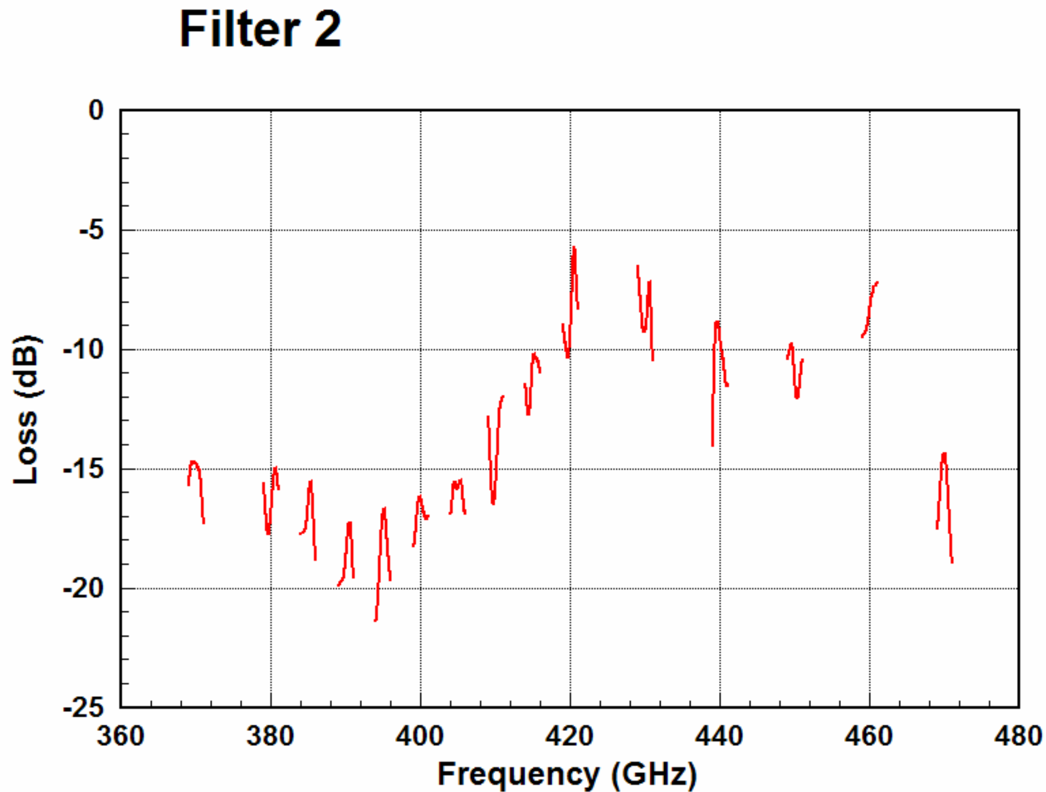

Fig. 14 Measured results of the micromachined cavity filter with the 20 µm wide iris walls.

In order to better understand some of the deep RIE and laser micromachining process effect we analyzed the slope effect on the iris walls, as well as the surface roughness for an identical 3-pole cavity filter operating in W-band. The band was chosen to facilitate future fabrication and measurements. A schematic of the 3-pole cavity filter that was simulated can be seen in Fig. 15. Fig. 16 shows the simulated filter response for a Delta value (slope width) of 0.06 µm. Figs. 17-19 show the simulated results as the Delta distance increases from 0.06 to 45 µm. As it is shown, when Delta increases the return loss decreases (more reflections), the filter center frequency decreases and the filter bandwidth increases. The Delta effect seems to be more pronounced on the filter center frequency and bandwidth. This should be taken into careful consideration when designing and fabricating such micromachined structures.

For the surface roughness issue, simulated results in W-band indicate that peak-to-peak values greater than 90 µm in the sidewalls start to cause a deterioration in the return loss.

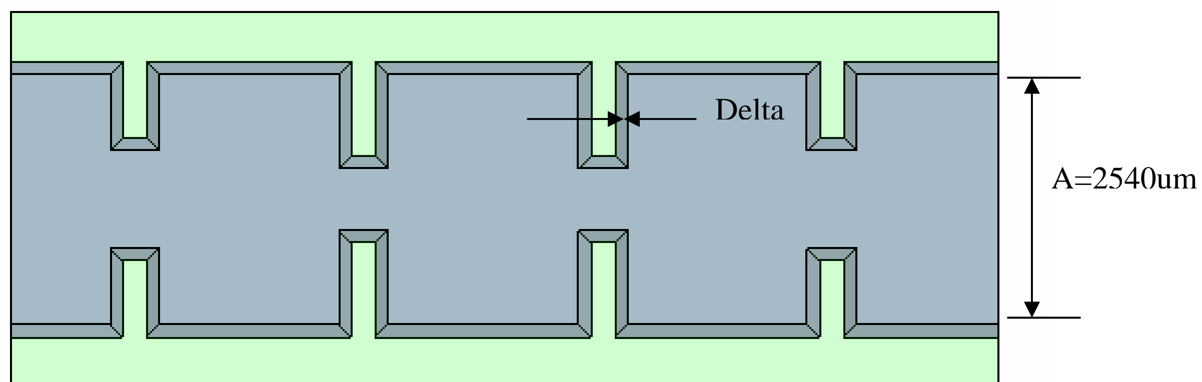

Fig 15. Top view of the half waveguide 3-pole cavity filter used in the HFSS simulations.

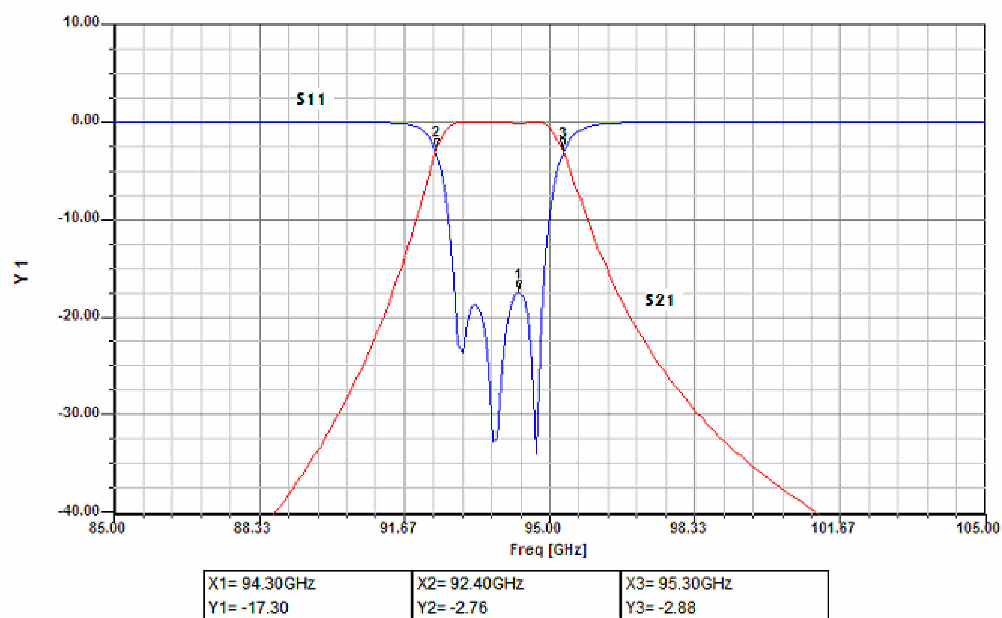

Fig. 16 Simulated 3-pole cavity filter response with a Delta of less than a 0.1 µm.

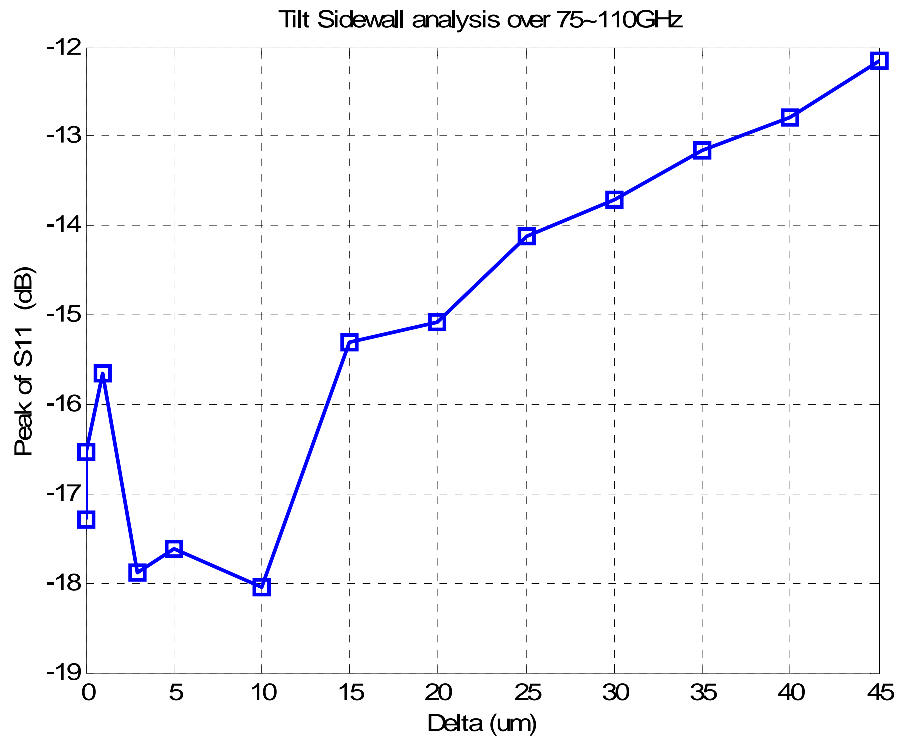

Fig 17. The relation between Delta and peak of S11

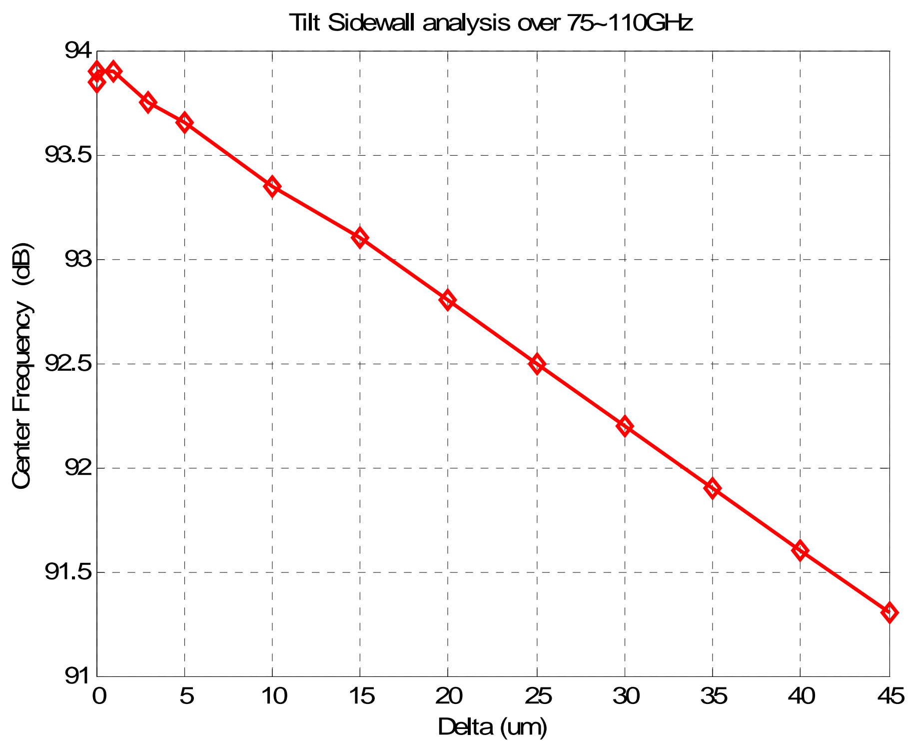

Fig 18. The relation between Delta and Center Frequency

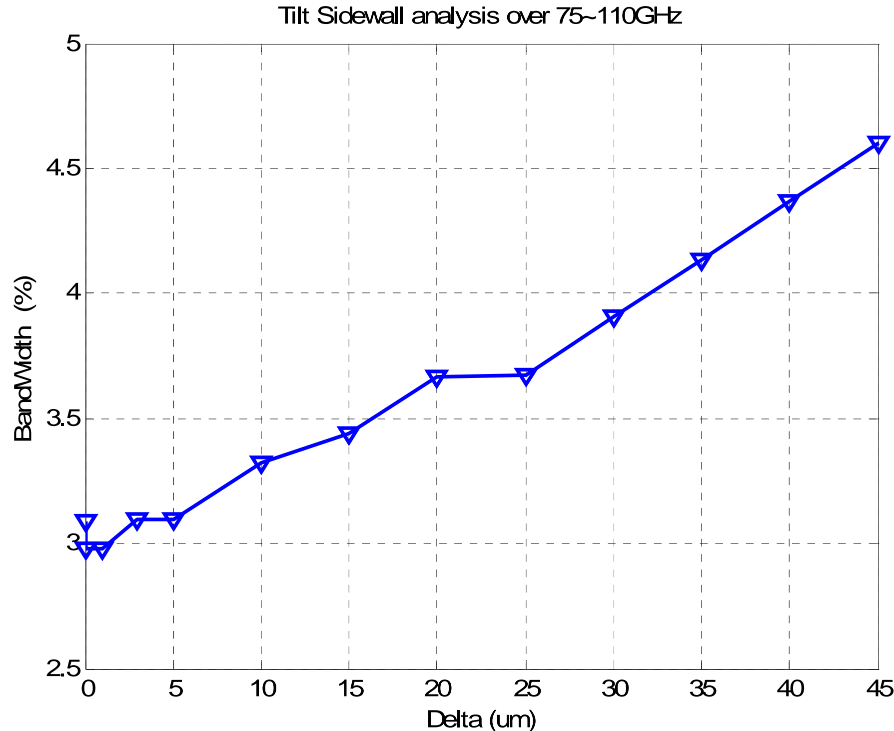

Fig 19. The relation between Delta and the filter bandwidth.

3. Analysis of Optimal Cut in "Split-Block" Micromachined Waveguides

Based on the experimental results thus far, we decided to investigate the micromachined waveguide performance based on cuts both in the H- and E-planes. This analysis will give us a better insight and understanding of the optimal configurations that need to be implemented with the "split-block" configuration technique. It should be noted that all the structures fabricated during the first year of this project were split in the H-plane.

Our analysis focused on longitudinally slotted W-band rectangular waveguides. A schematic of such waveguide is shown in Fig. 20. The specification of the simulation is shown in the following table. Some assumptions are made before the simulation. First, the waveguide is made of 2 μm thick gold. Vacuum is within the waveguide and out of the waveguide. Second, the boundary of the outer box is a radiation boundary.

Parameter	Value
a	2540 um
b	1270 um
d	2~10um(H-Plane Split)
Length	4000 um
Frequency	75~120GHz
Radiation Box Dimension	5650 x 4000 x 2800 um

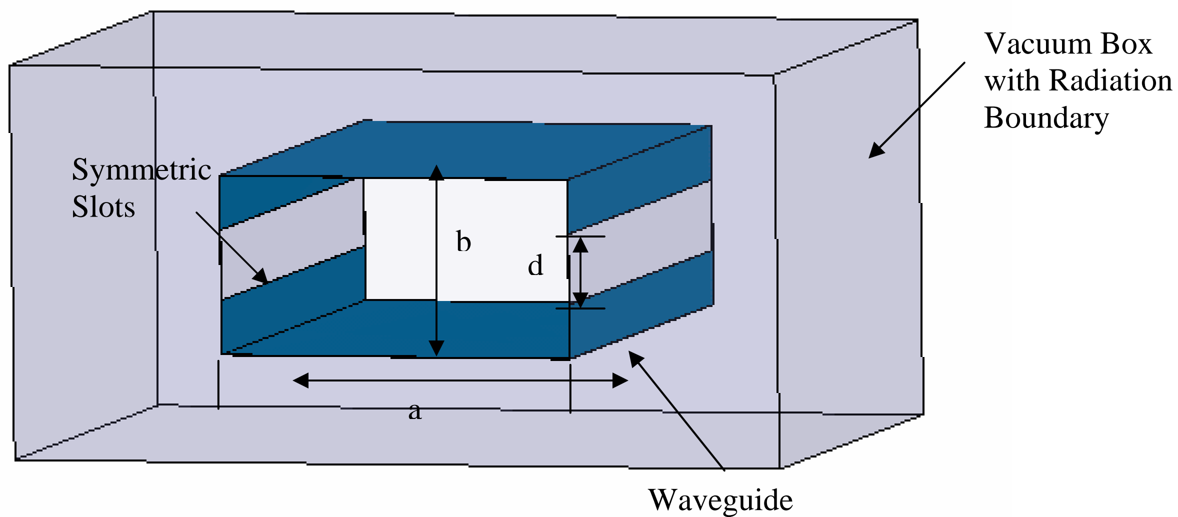

Fig. 20. The slotted rectangular waveguide.

The first simulation result is shown in the Fig. 21. The relative delivered power is very poor even with small slot width d.

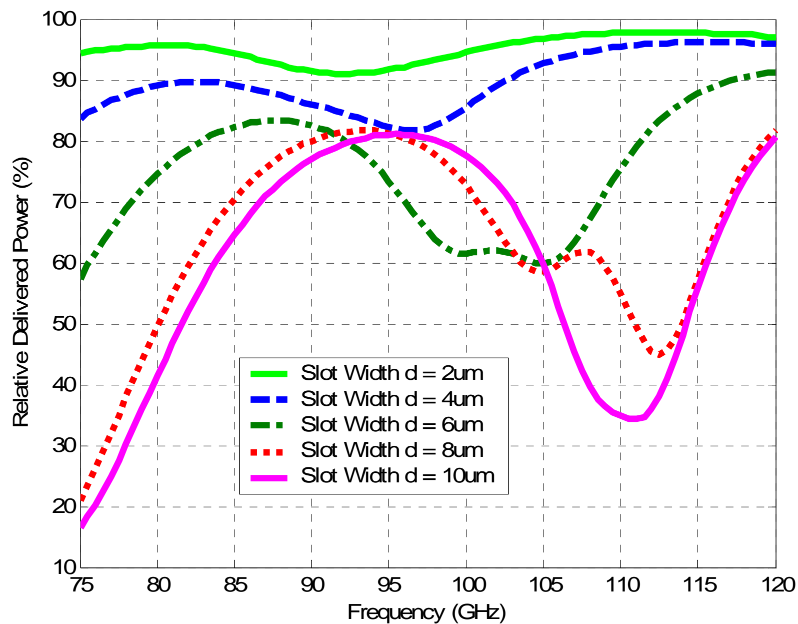

Fig. 21 Relative power handling capability with normalized slot width.

According to the results of Fig. 21, the split on the narrow wall of the waveguide shows a sensitive response. The loss can be very high even with a narrow slot. One twentieth of the human hair slot (10 μm) at 75 GHz reduces the power handling capability to 16.5%. The power handling capability is almost lost with a small slot width. But, in the fabrication, two symmetric parallel plates can be made on both sides of the waveguide. Such a configuration also replicates the fixture/package effect. The schematic is shown in the following figure:

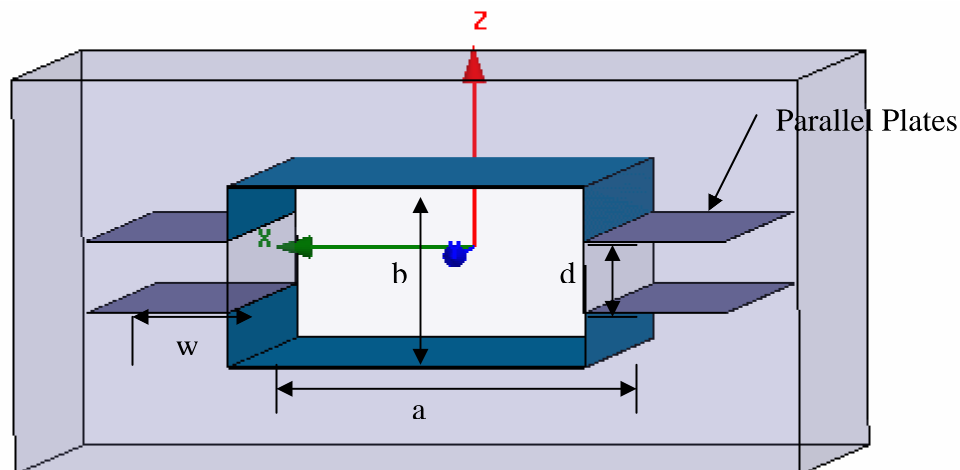

Fig. 22. The slotted rectangular waveguide with parallel plates.

The assumptions are the same as those for Fig. 20. The normalized slot width equals d/b. The specification of the simulation is shown in the following table:

Parameter	Value
a	2540 um
b	1270 um
d	0~1270um(H-Plane Split)
w	1000 um
Length	4000 um
Frequency	75~120GHz
Radiation Box Dimension	5650 x 4000 x 2800 um
normalized slot width	d/b

Fig. 23 shows the power handling capability of the waveguide in W-band. With the same normalized slot width, higher frequencies can deliver more power than lower frequencies. At the same frequency, the larger the slot width the lower the power

handling capacity until the normalized slot width (T) is larger than 0.6. The power handling capacity is 85.4% at 75GHz and 93.1% at 110GHz with 50um width slots. It is not clear yet why the relative delivered power increases a little bit when T is larger than 0.6.

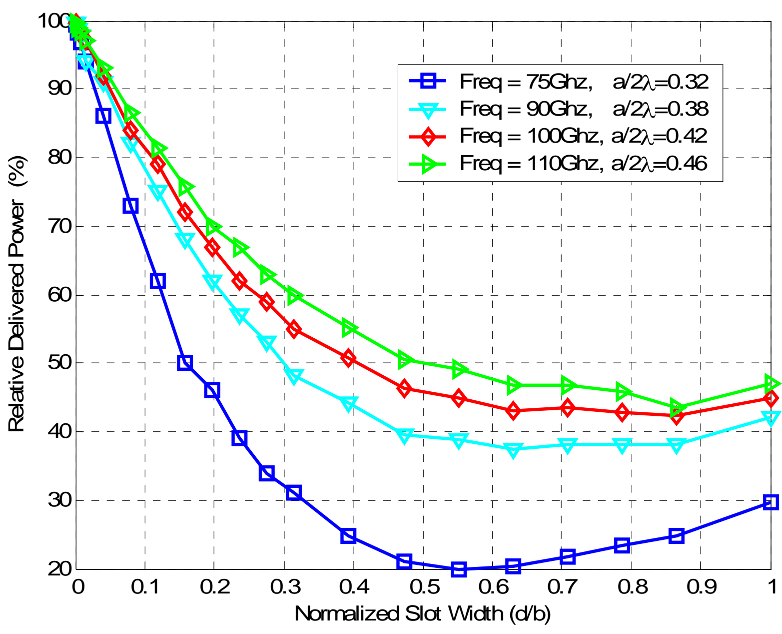

Fig. 23 Relative power handling capability with normalized slot width.

The next two simulation results show the trend of relative delivered power with the increase of frequency. One is for a large slot width, while the other one is for a small slot width.

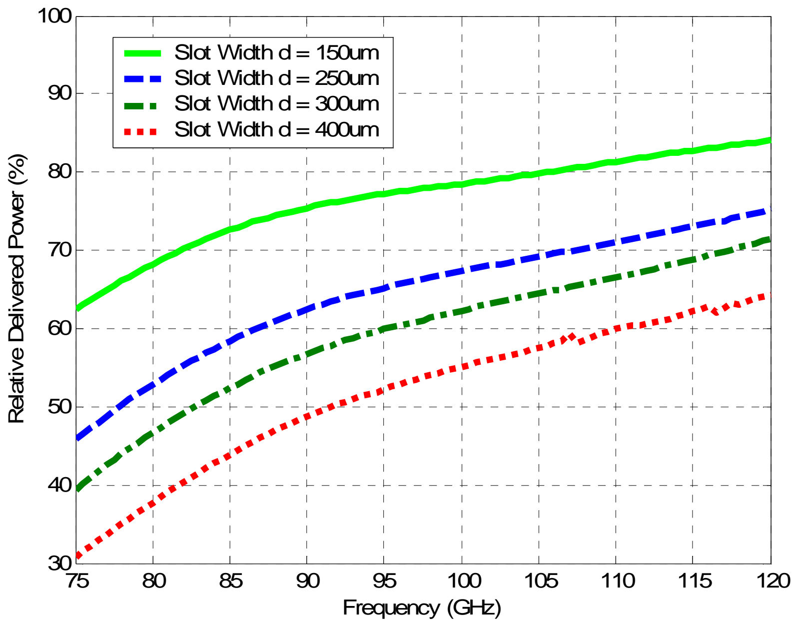

Fig. 24 Relative power handling capability for large slot width, d.

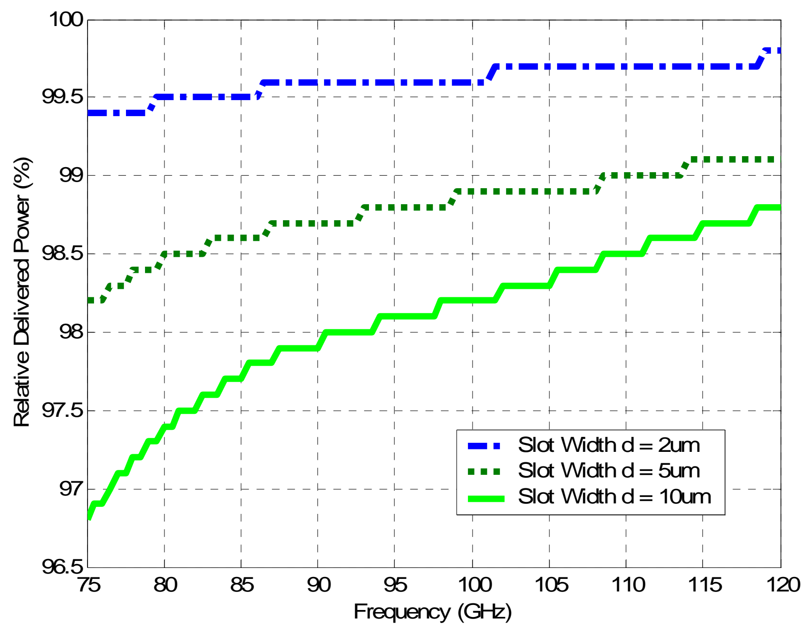

Fig. 25 Relative power handling capability for small slot width, d.

The last simulation result in this section shows the |S11| and |S21| at 75GHz.

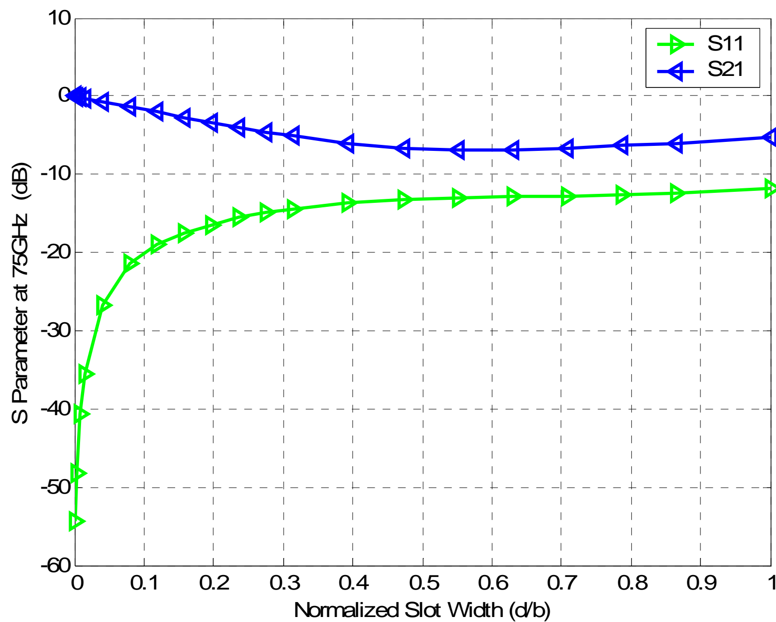

Fig. 26 S-Parameters with Normalized Slot Width.

According to the previous simulated results, the parallel plates greatly enhance the power handling capability. Comparing Fig. 21 with Fig. 25, we found that the performance of the waveguide becomes much better in the presence of the parallel plates.

Our next task is to investigate how wide the parallel plates should be to get a good power handling capacity. Figure 27 shows the simulation results under the same specifications as those of Fig. 22. The simulation results show that the width of the parallel plates should be not less than 1000 μm. The fixture that we use to make the s-parameter measurements of the micromachined waveguides provides enough width to ensure maximum power delivery through the components. Of course, this issue will not exist once the micromachined parts are bonded together with a reliable bonding technique.

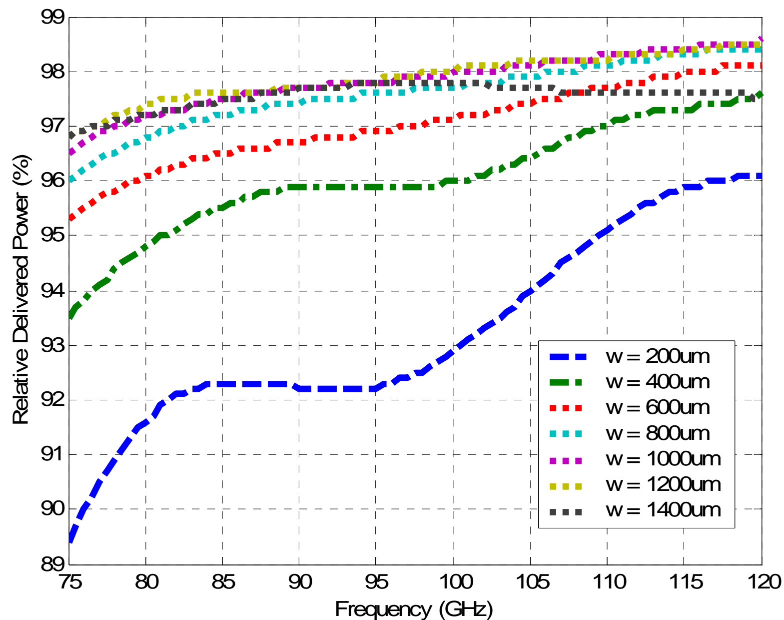

Fig. 27 Relative delivered power vs**.** the width of the parallel plates.

In order to compare the split on the E-Plane and on the H-Plane, similar simulations are performed using an E-Plane split with parallel plates. The simulation parameters are summarized in the Table below. Results are shown in Figs. 28-29.

Parameter	Value
a	2540 um
b	1270 um
d	0~1270um(E-Plane Split)
w	1000 um
Length	4000 um
Frequency	75~120GHz

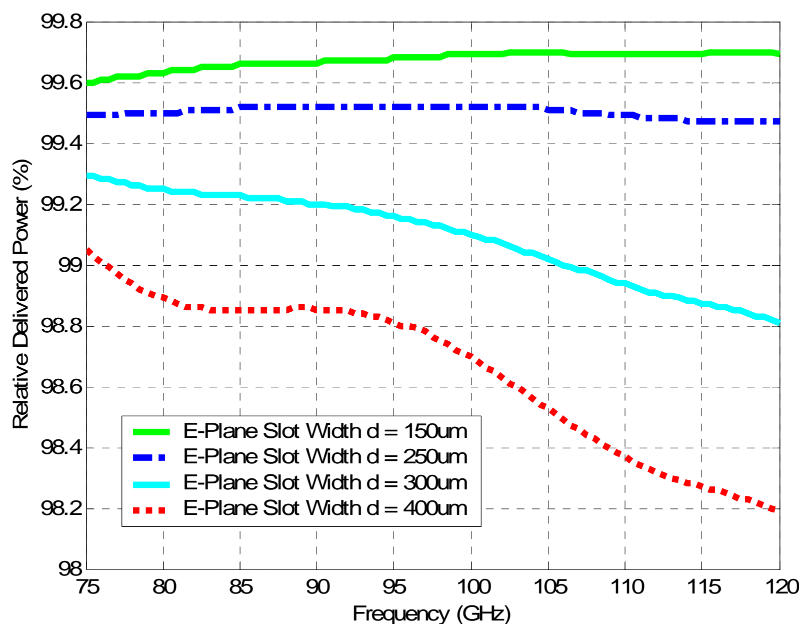

Fig 28. Relative power handling capability vs. frequency for large slot width and E-plane split.

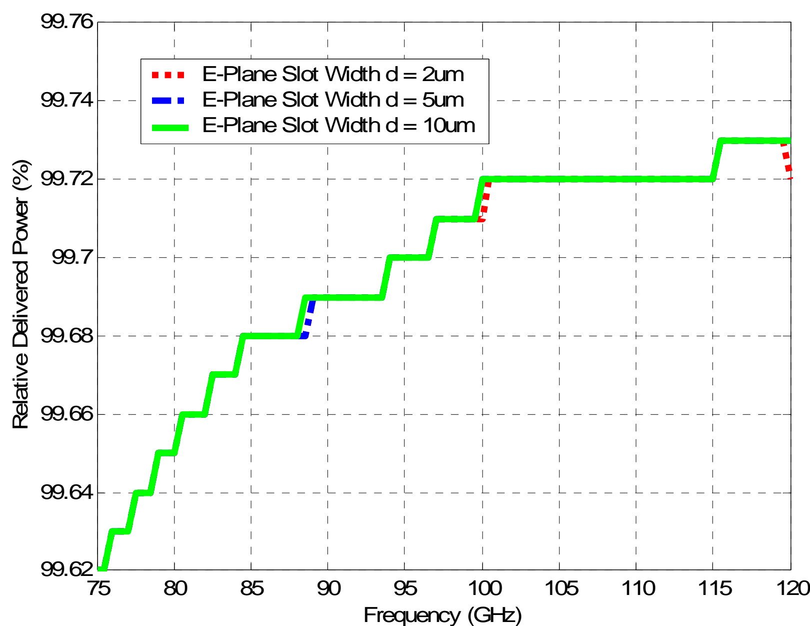

Fig. 29 Relative power handling capability vs. frequency for small slot width and E-plane split.

Comparing Figs. 28 and 29 with Figs. 24 and 25, we found that the E-Plane split is better than the H-Plane split. The following two figures show the difference of power handling capacity between the E-Plane and H-plane split. When the slot width is small, the E-Plane split is a little bit better than the H-Plane split. But, when the slot width is large, the E-Plane split is much better than the H-Plane split.

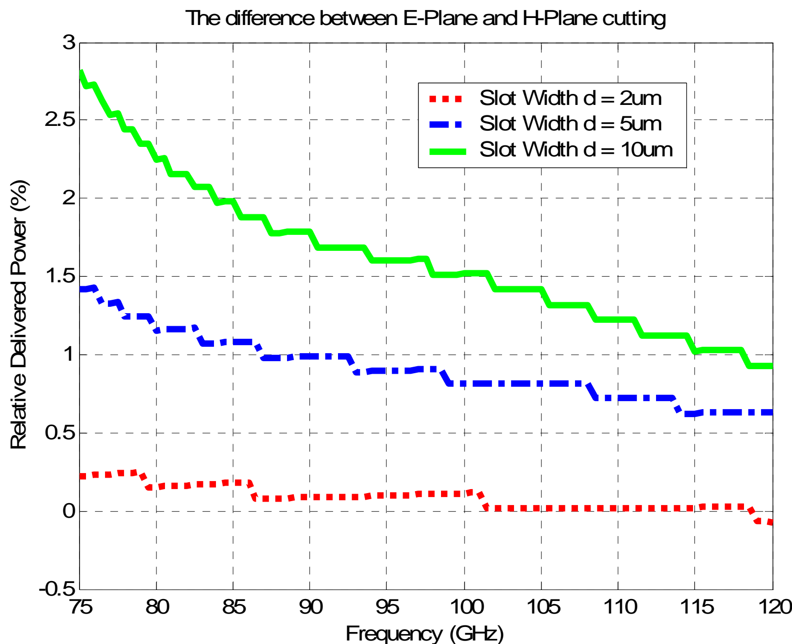

Fig. 30 Relative power handling capability between E- and H-plane splits for small widths, d.

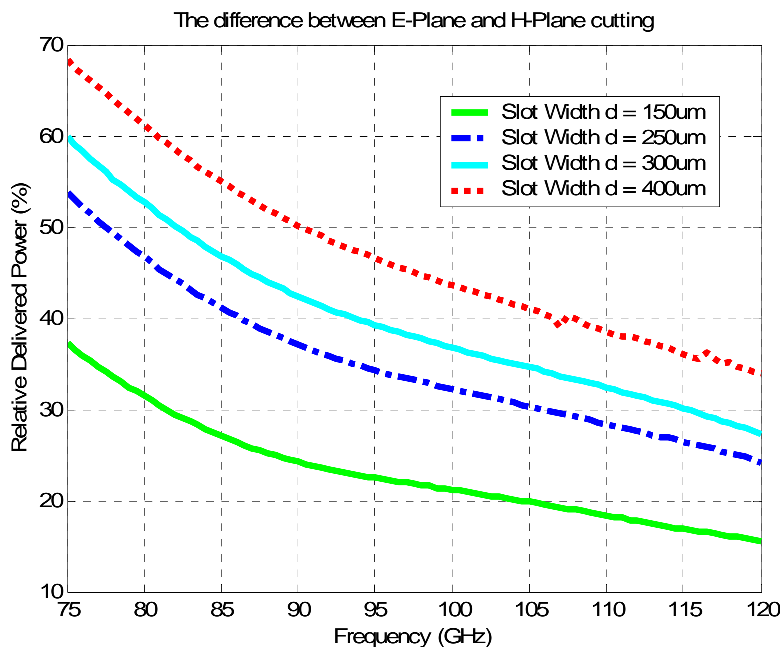

Fig. 31 Relative power handling capability between E- and H-plane splits for large widths, d.

The conclusion of the above simulations is that if a minimal or non-existent gap between the "split block" components cannot be achieved via the package/fixture or the bonding techniques, the waveguides will exhibit increased insertion loss due to leakage if the H-plane split is used. For a more robust design, the simulations indicate that an E-plane split is better.

4. Analysis of Meander Micromachined Waveguides in W-Band and 400 GHz.

Meander micromachined waveguides were theoretically analyzed both in W-band and around 400 GHz for optimal response. Fig. 32 shows the schematic of the simulated structure, along with the parameters of interest.

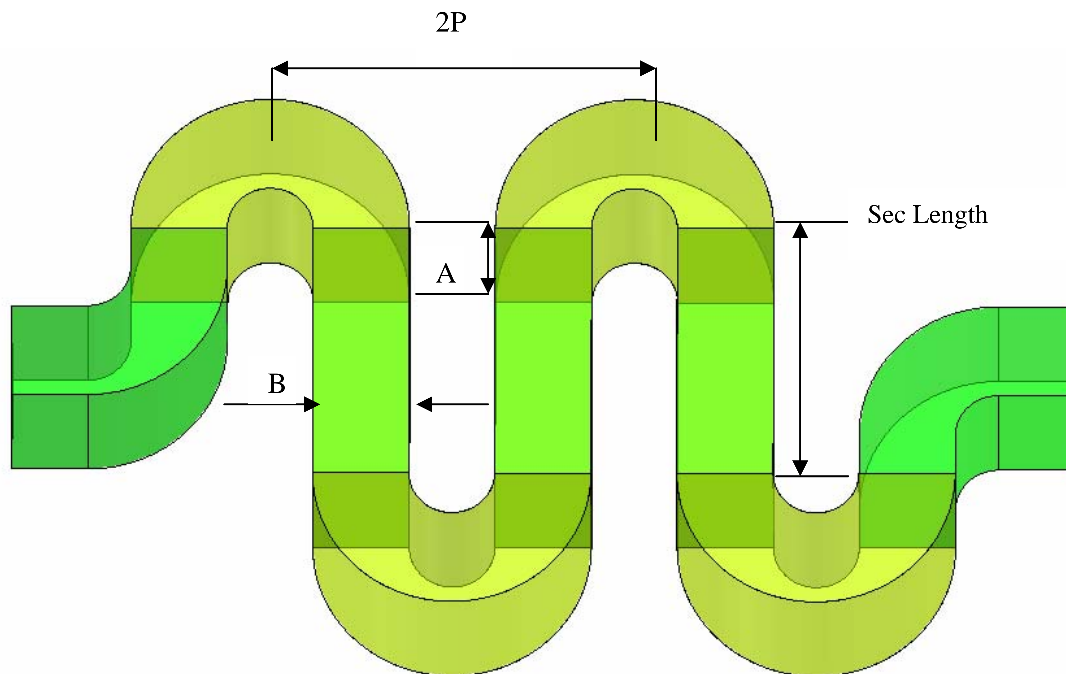

Fig. 32 Schematic of a meander micromachined waveguide to be used in high-frequency power amplifiers.

The table below summarizes the parameters that were used in the full-wave simulations.

Parameter	Value
A	2540 um
B	50~1270um
P	1800 um
SecLength	3500 um
Frequency	75~110GHz

Simulated results are shown in Fig. 33. It can be observed that for a B value ranging between 200 and 800 μm the return loss is higher than 20 dB.

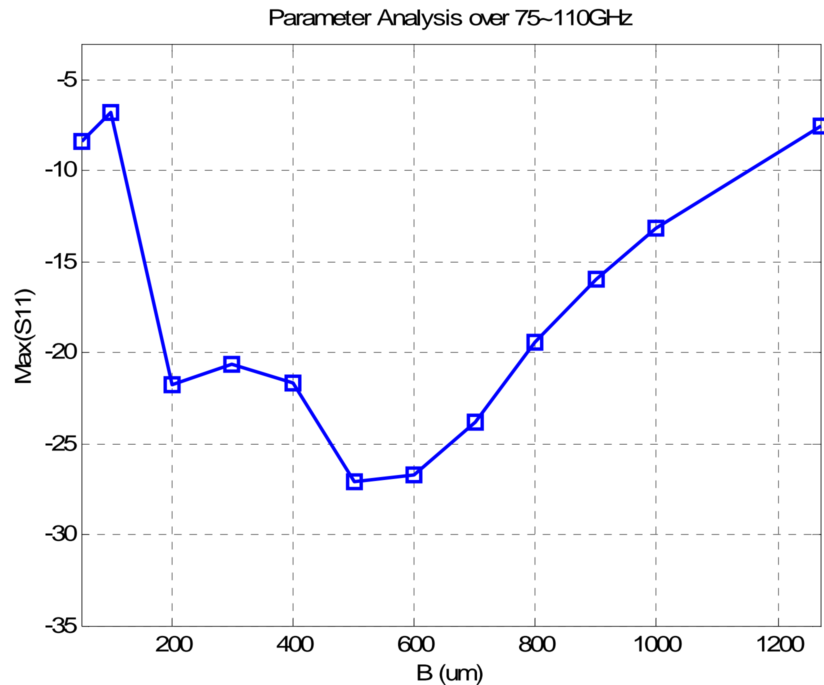

Fig. 33 Maximum S11 vs. parameter "B" for meander waveguide operating in W-band.

The next step was to analyze the waveguide performance in terms of the "section length". The table below shows the parameters used and the results are shown in Fig. 34. As it is shown the return loss is much more sensitive to this parameter and it should be chosen carefully in order to get the best possible results.

Parameter	Value
A	2540 um
B	1270um
P	1800 um
SecLength	2000~9000 um
Frequency	75~110GHz

The last set of simulations was with respect to parameter "P". The table below shows the range of variables used, while Fig. 35 shows the results.

Parameter	Value
A	2540 um
B	1270um
P	1400~9000 um
SecLength	3500 um
Frequency	75~110GHz

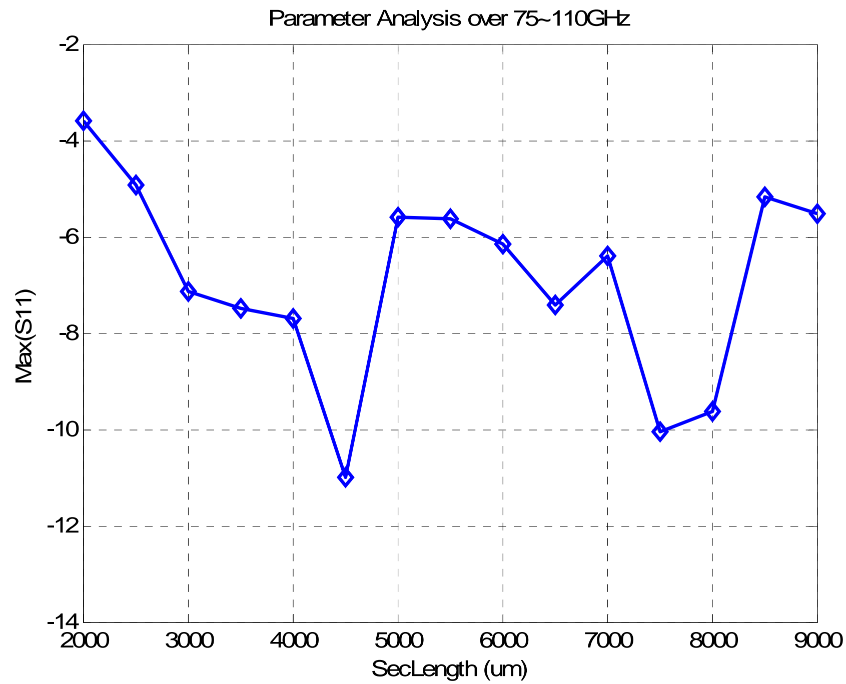

Fig. 34 Maximum S11 vs. parameter "SecLength" for meander waveguide operating in W-band.

Fig. 35 indicates that as the parameter "P" increases, the maximum return loss gets higher.

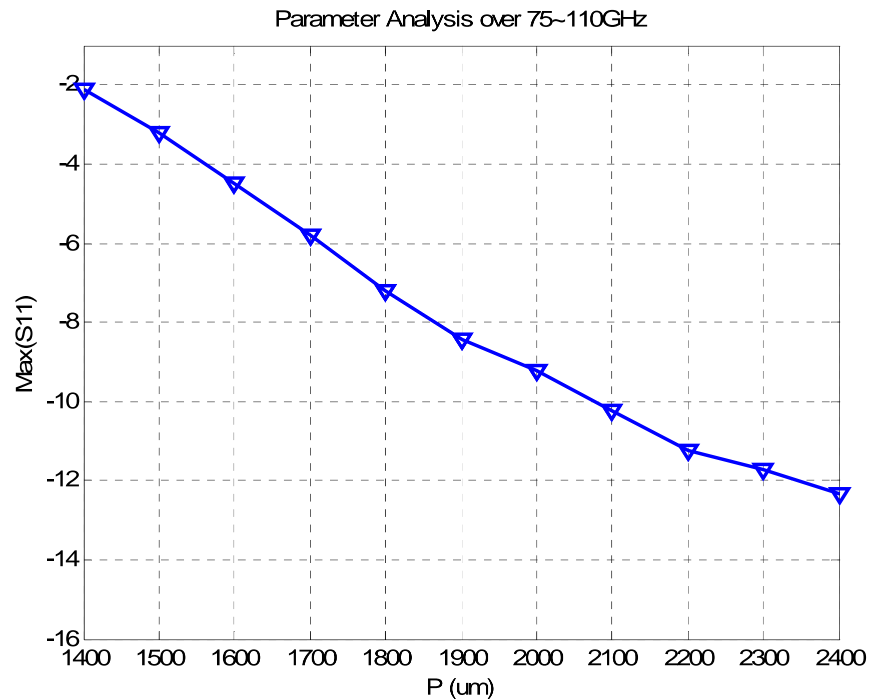

Fig. 35 Maximum S11 vs. parameter "P" for meander waveguide operating in W-band.

A schematic of a 400 GHz folded waveguide along with simulated results is shown in Figs. 36-37. The waveguide cross-section is 167 µm x 334 µm. Photos of the fabricated micromachined folded waveguides are shown in Fig. 38. Measurements of the folded waveguides will be performed in early 2006.

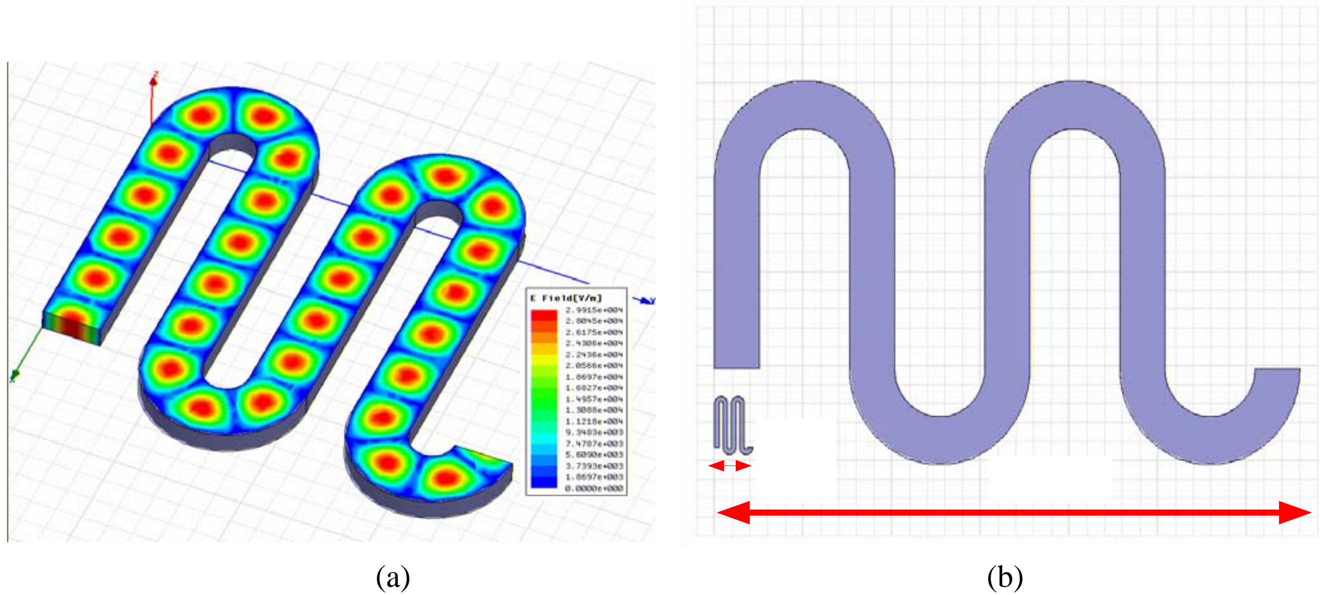

(a) (b)

Fig. 36 a) E-field pattern of a 400 GHz folded waveguide and b) waveguide top view and dimensions.

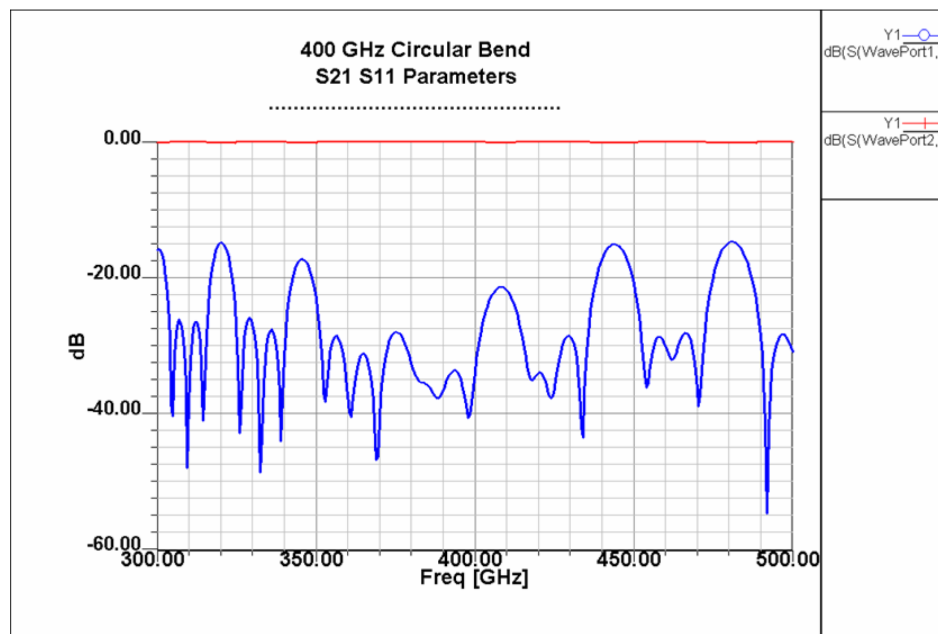

Fig. 37 Simulated results of the 400 GHz folded waveguide.

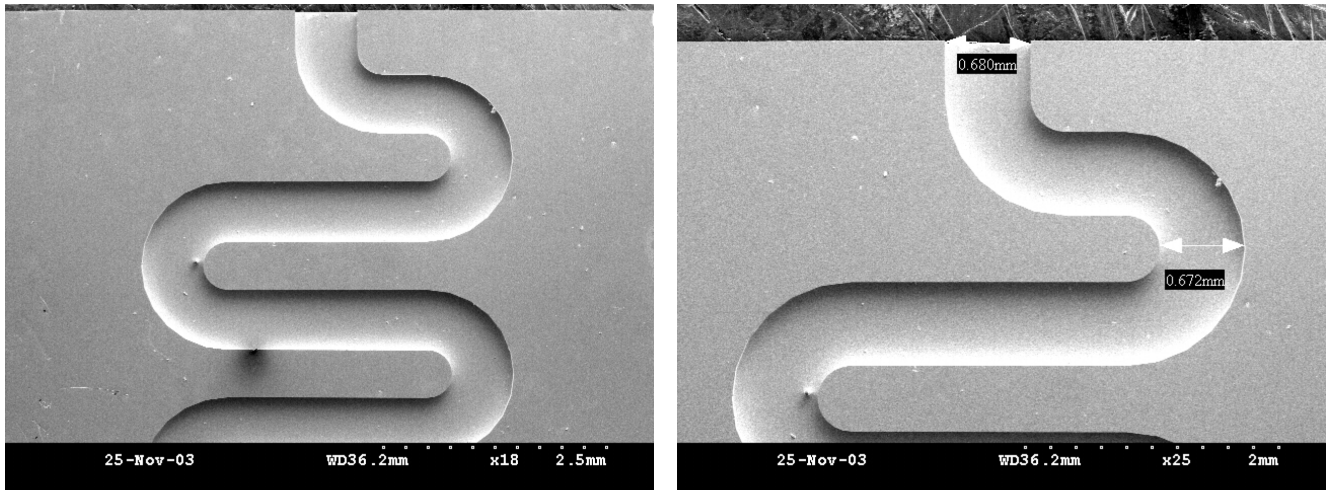

Fig. 38 a) Photo of "split-block" folded waveguide and b) close-up with dimensions. The waveguides were fabricated using the deep reactive-ion etching technique.

5. Analysis of Meander Micromachined Waveguides and Transitions in W-Band

In order to measure the meander micromachined waveguide components, we designed and optimized appropriate waveguide transitions to interface with WR-10 waveguides used in W-band measurements systems. A schematic of a tapered transition is shown in Figs. 39-41. Different taper functions were investigated: linear, exponential and inverse square-root.

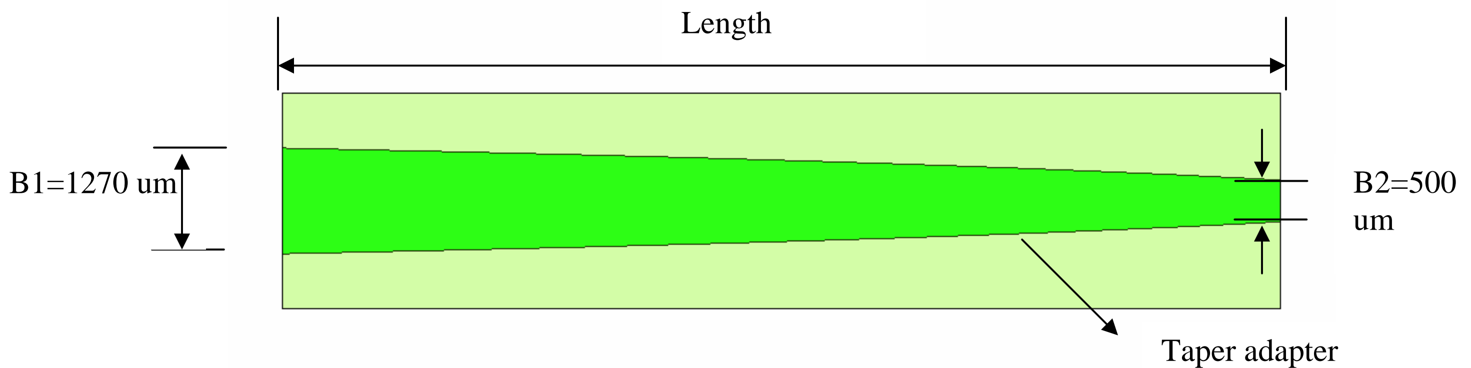

Fig. 39 Top view of the waveguide adapter

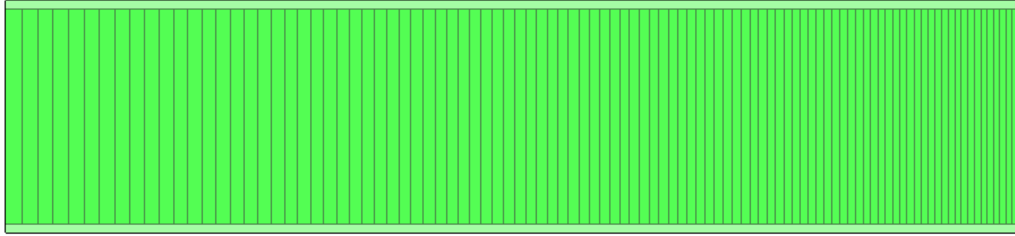

Fig. 40 Front view of the waveguide adapter

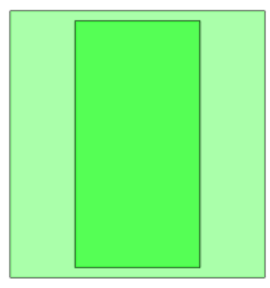

Fig. 41 Left view of the waveguide adapter

The W-band waveguide taper adapter was simulated with the following parameters shown in the table below:

Parameter	Value
A	2540 um
B1	1270um
B2	500um
Length	1000~12000 um
Frequency	75~110GHz
Taper Shape	Exponential, Linear, Inverse-Square-Root

Fig. 42 shows the maximum S11 vs. taper length for the various taper designs. It can be seen that a linear taper, which can be easily designed, produces high return losses (RL>20 dB) for lengths longer than 5 mm. For taper lengths longer than 6 mm all taper designs provide high return loss. Figs. 44-46 show the simulated s-parameters for the entire assembly to be measured in W-band (meander waveguide plus transitions). A schematic of the entire structure is shown in Fig. 43. The simulated results indicate that very low loss (~0.1 dB) can be achieved.

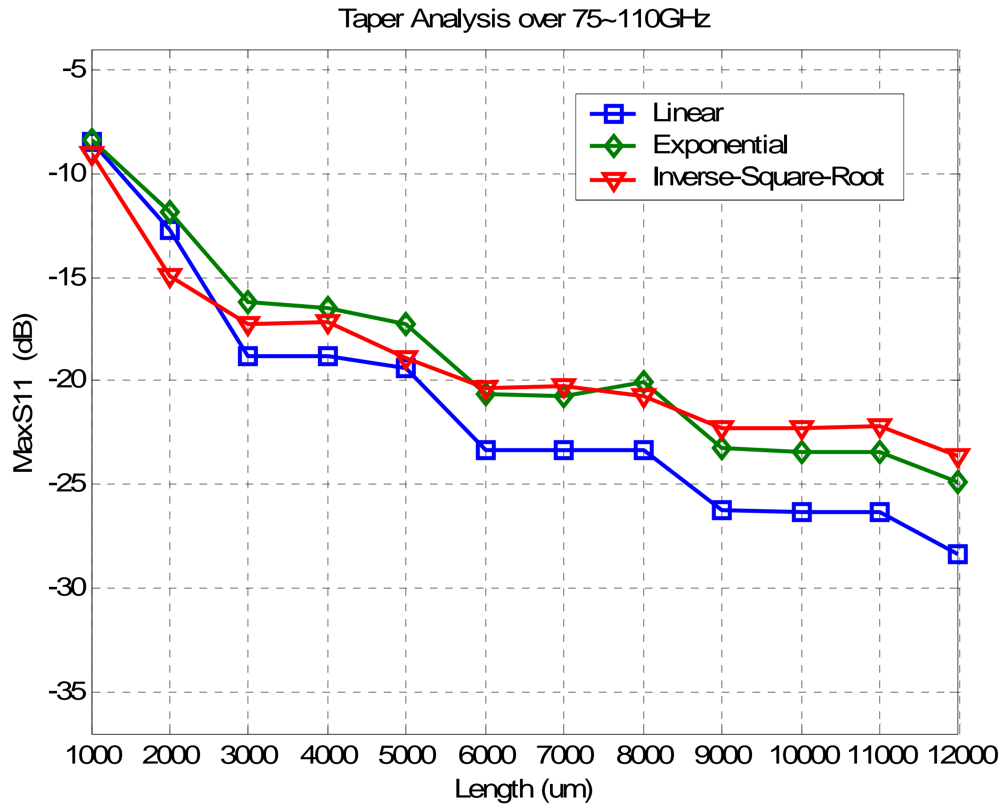

Fig. 42 The maximum S11 for various taper designs vs. length in W-band.

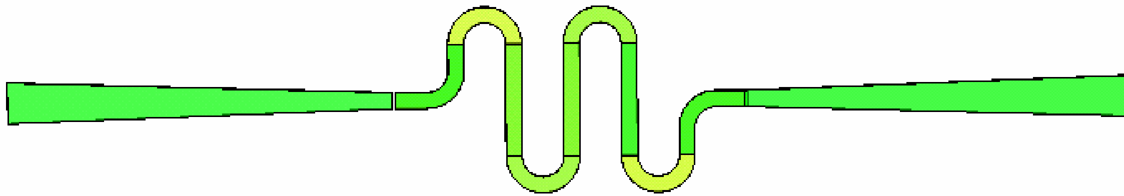

Fig. 43 Schematic of meander micromachined waveguide with transition tapers for measurements in W-band.

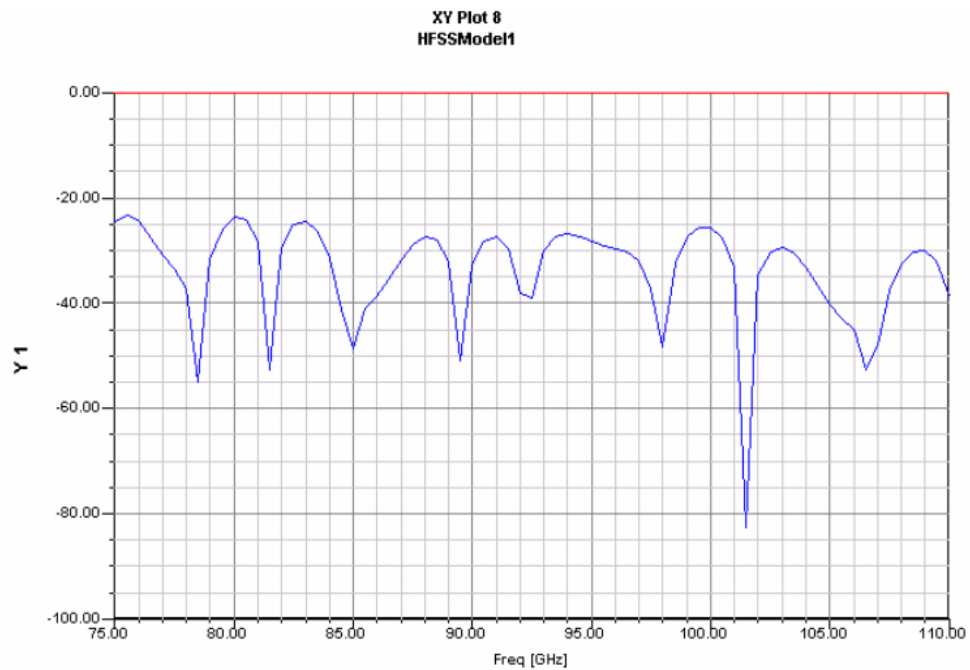

Fig. 44 S11 (blue line) and S21 (red line) of the meander waveguide with linear taper vs. frequency.

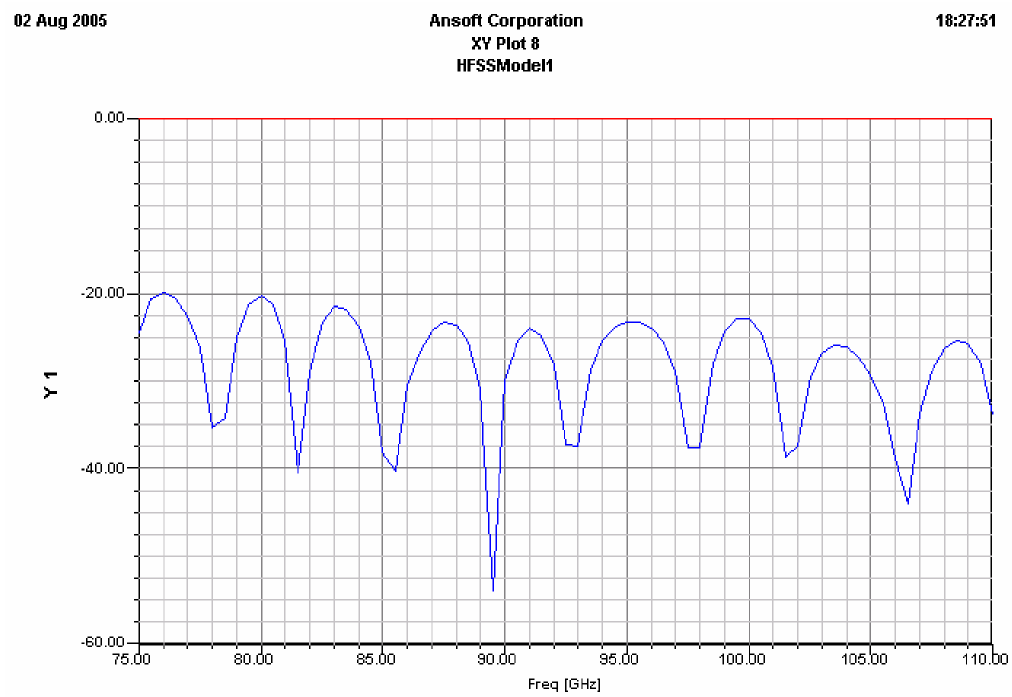

Fig. 45 S11(blue line) and S12(red line) of the FWTWT with exponential taper vs. frequency

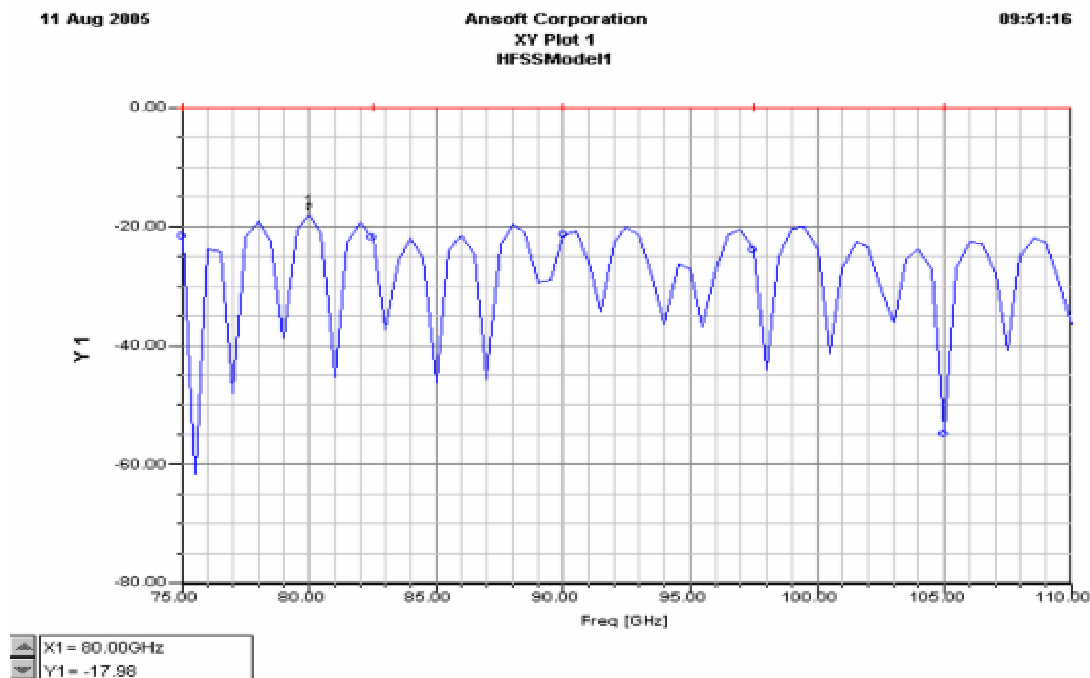

Fig. 46 S11(blue line) and S12(red line) of the FWTWT with inverse square taper vs. frequency.

6. Development of Silicon Micromachined THz Multiplier

6.1 Introduction

When considering circuit design in the range of 100 GHz to 1-2 THz, the conducting medium of choice is often rectangular waveguide. As frequency goes higher, the fabrication of the rectangular waveguide by traditional metal machining techniques becomes costly and requires a great deal of skill and expensive equipment. In an array type of application or when multiple copies are needed, traditional machining can be very costly. An alternative to traditional metal machining is the use of micromachining on a silicon substrate. Silicon micromachining provides much greater dimensional control and can readily be adopted for array or multiple copy production.

We have successfully explored the use of silicon micromachined waveguide at 400 GHz and in the W-Band frequency range utilizing straight waveguides and filters [1-3]. In this work, we take the next step by developing a common component utilized in the sub-millimeter realm, the frequency multiplier.

The frequency multiplier waveguide is formed entirely of metallized micromachined silicon. For the active portion of the multiplier we utilized a previously proven heterostructure barrier varactor (HBV) [4-6]. Utilizing this particular device eases the overall fabrication of the design as no idler circuit is necessary since only odd order harmonics are produced and it is a bias-less design, so no additional design is necessary to provide bias to the circuit.

6.2 Design and Fabrication

In traditional multiplier block fabrication, the block is split equally in the E-plane. Splitting in the E-plane helps to avoid any current leakage that might be experienced when splitting in the H-plane when gaps in the seam might be present. We split the block along the E-plane into two halves. Each half has three different depths, two for the WR-10 input and WR-3 output waveguide, and a third depth for the channel. The basic shape for the multiplier block is shown in Fig. 47.

The silicon is etched using a Bosch Deep Reactive Ion Etching (DRIE) process. When using a DRIE etching process, it is very difficult to etch multiple depths into a single wafer. With this consideration, the most straight forward way to form the complete multiplier block is by dividing each half of the block into three slices, with the block having a total of six layers.

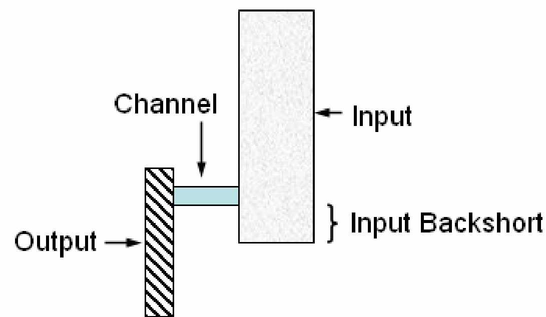

Fig. 47 Basic layout of the multiplier waveguide block.

For each half of the block, three separate depths are needed (see Fig. 47): The Input section will need a depth of 1.27 mm, the output section will need a depth of 0.432 mm; the Channel will have different depths depending on which half of the block, 0.117 and 0.056 mm respectively. To accomplish this we utilize 2 different low resistivity wafer thicknesses, a 400 um thickness to form the channels for the HBV circuit and 525 um thickness to form the rest of the waveguides (see Fig 48). For the 'A' wafer, the top side is etched to the desired channel depth where the HBV circuit will be mounted. A backside alignment is then performed which follows with a bottom side etching through the entire wafer. The 'B' wafer has a top side etch to finish the depth of the output waveguide, then the backside alignment is performed and the bottom side etch is performed all the way through the wafer. Finally, the 'C' wafer is etched to finish the depth of the input waveguide and then a backside alignment is performed and the bottom side is etched through to release the chip from the wafer. The exact process is performed for the opposite half of the block, with a different channel depth in wafer 'A'.

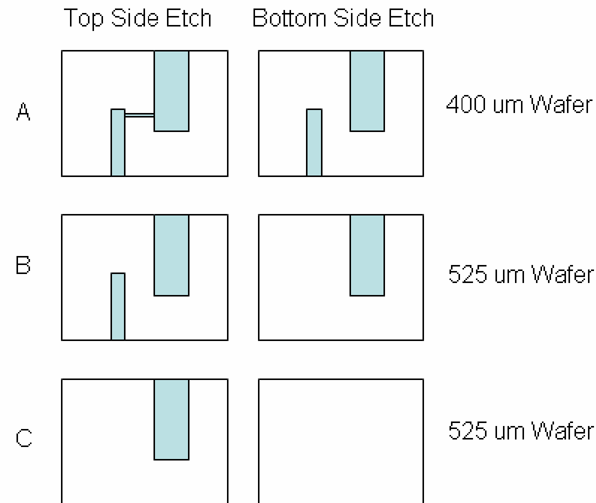

Fig. 48 The approach to etching 3 wafers to form one-half of the silicon waveguide block. The shaded portions indicate where the etching is performed.

The last step in the fabrication is metallization. Each of the pieces is metalized using a sputtering technique which is composed of Titanium (for adhesion), Copper (for conduction) and Gold (to prevent oxidation of the Copper) with a total thickness of 4 um. Both sides receive the same amount of metallization insuring good coverage in the waveguide channels.

6.3 Assembly

The silicon pieces are mounted in a brass block in order to facilitate the measurement. Two alignment pins are seated in the block to align the silicon pieces as they are stacked vertically. After three silicon pieces are stacked, the HBV circuit is mounted in the channel using UV-cured epoxy. A photo of one half of the block with the diode circuit mounted is shown in Fig 49. The remaining silicon pieces are stacked on top of the HBV circuit. Fig. 50 shows the silicon block with four pieces to detail how the block is formed with the HBV circuit inside. Finally, the cover of the brass mounting fixture is applied and tightened with screws. Each side of the brass fixture is patterned with a standard waveguide flange pattern accounting for the thickness of the silicon pieces. The final assembly is shown in Fig. 51. A closer view of the WR-10 and WR-3 waveguide openings is shown in Fig. 52.

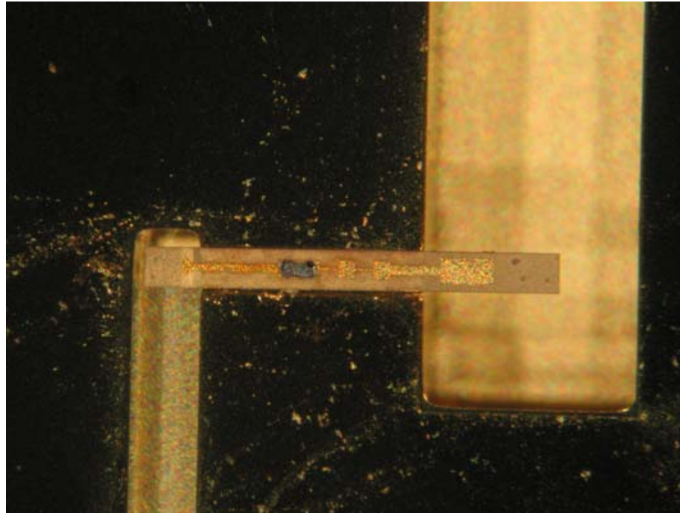

Fig. 49. Photo of the silicon waveguide block (3 layers) showing the HBV circuit mounted.

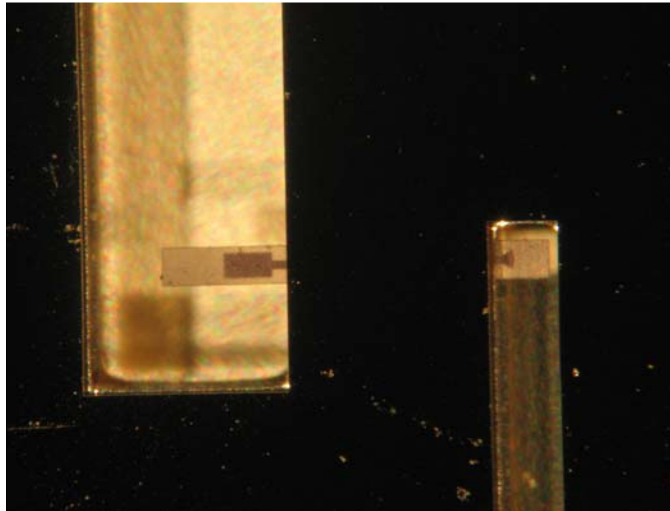

Fig. 50. Photo of the silicon waveguide block (4 layers) showing the HBV circuit mounted with the next silicon layer on top of the circuit

Fig. 11. Photo of the assembled Silicon waveguide block.

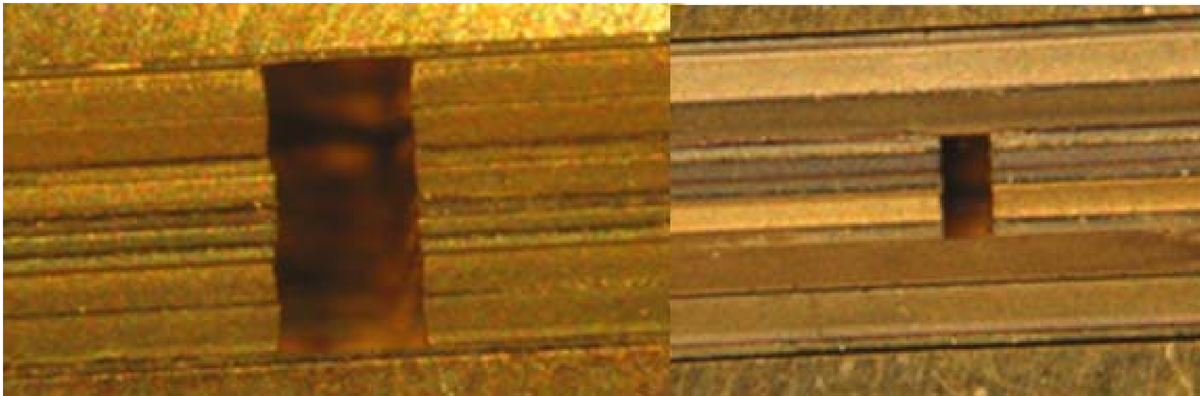

Fig. 52. Photo of the input (left) and output (right) waveguide openings in the Silicon waveguide block.

6.4 Measurements

The input signal is generated by a 90 GHz frequency doubler (Virginia Diodes, Inc) that is driven by a 45 GHz power amplifier. This signal is fed through a W-Band direct reading attenuator to control the delivered input power. Next the signal is fed through a directional coupler configured for reflection measurements. The output of this coupler is measured using an HP W-Band 8486A power sensor to allow determination of the amount of power delivered to the multiplier block.

After the measurement system is calibrated, the silicon waveguide block is attached to the output of the coupler. The output of the silicon waveguide block is fitted with a WR-3 to WR-10 transition and is fed into an Erickson power sensor attached to an Erickson Instruments Ltd. PM-1B Power meter.

The testing was performed with an input signal ranging from 86.5 GHz to 88 GHz. The input power was swept from a range of 40 mW up to 120 mW depending on frequency. It was

determined that the peak output power of the assembly occurred at 87 GHz, corresponding to an output of 261 GHz. The output power versus input power and input power versus conversion efficiency are shown in Fig. 53 and Fig. 54, respectively.

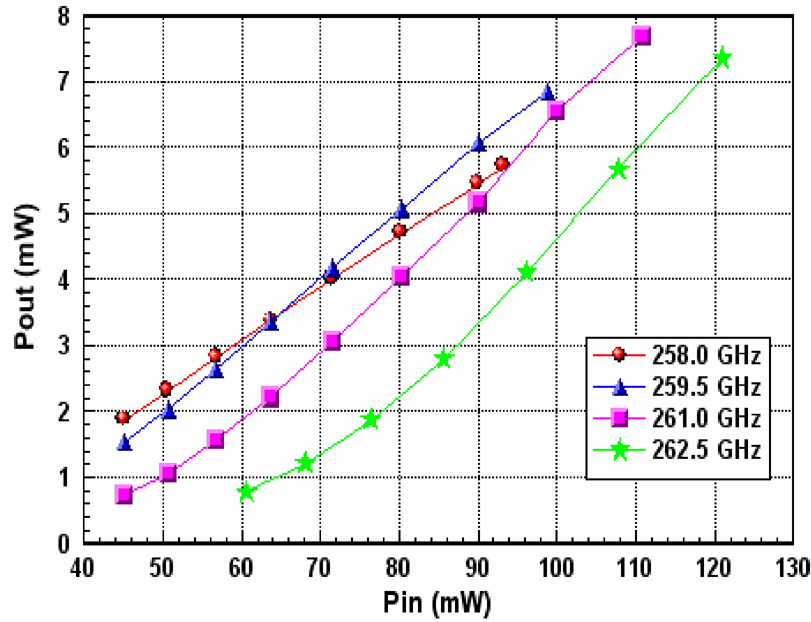

Fig. 53. Input power versus output power at multiple frequency points for the silicon waveguide block.

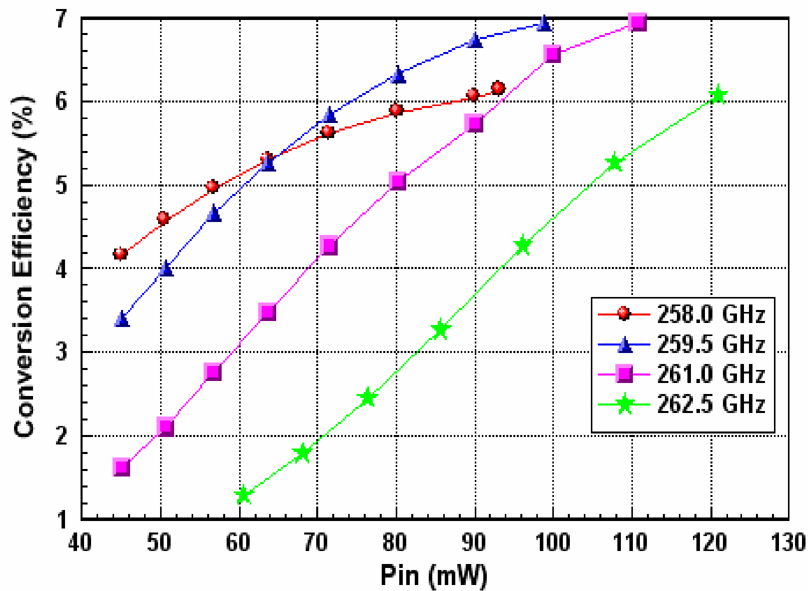

Fig. 54. Input power versus conversion efficiency at multiple frequency points for the silicon waveguide block.

After determining the peak input to be 87 GHz, the block was driven at to the maximum available power of 120 mW to determine the maximum output power and conversion efficiency.

The result is shown in Fig. 55 with a maximum output power of 7.7 mW at an efficiency of 6.9%. The input return loss was also measured at 93 GHz and is plotted in Fig 56.

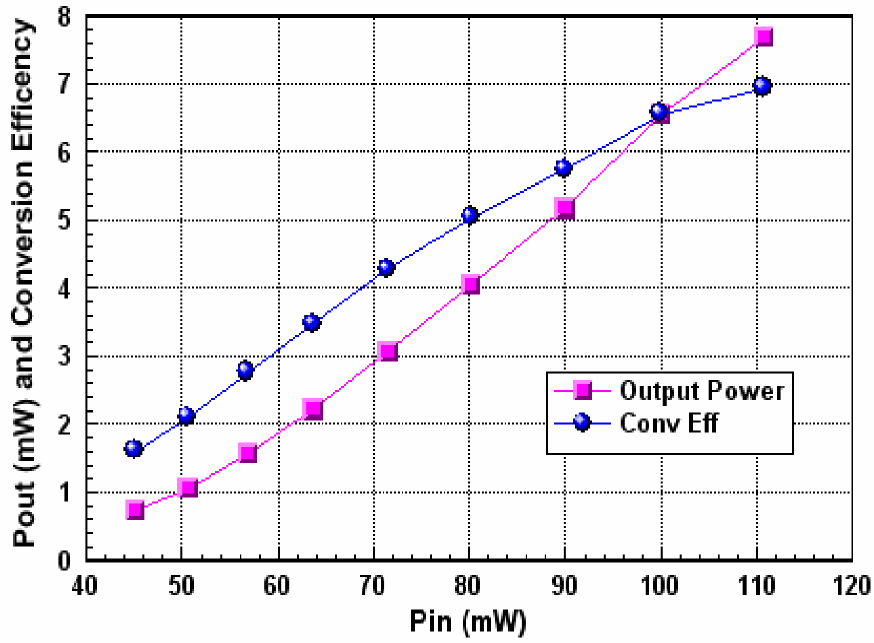

Fig. 55 Output power and conversion efficiency versus input power at 261 GHz (peak output power).

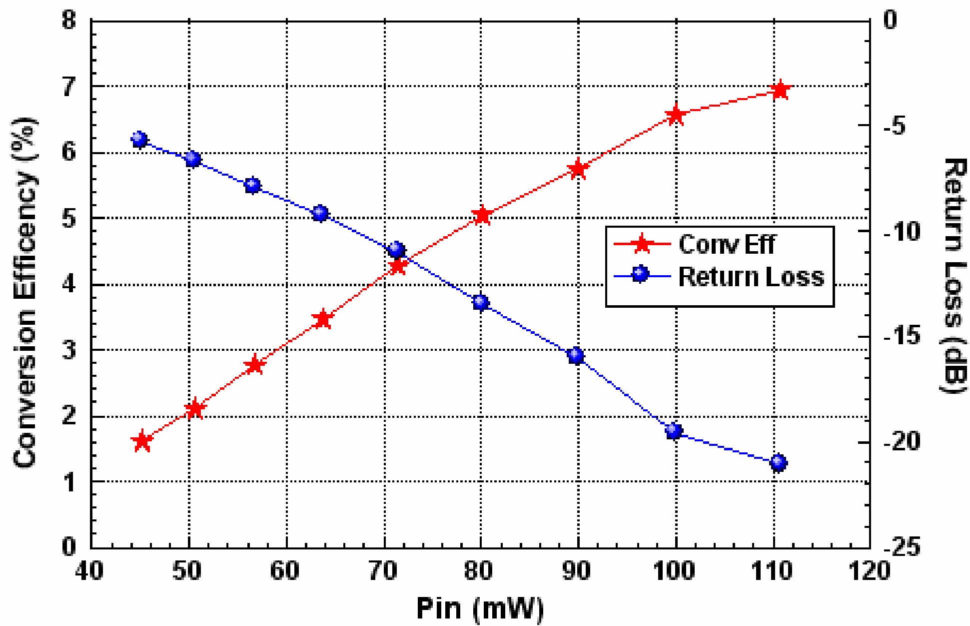

Fig.56 Output power and conversion efficiency versus input power at 261 GHz (peak output power).

The performance of the silicon block is similar in performance to the metal block used in [4], 6.5 mW of output power and 6.5% efficiency at 271.5 GHz. One item to note is the difference frequency response, in the peak output power, 261 GHz versus 271.5 GHz.

It should be noted that multiple layers used to construct the block could cause problems. Although a seam has little impact in the center of an E-Plane split, it becomes problematic if seams are present away from the center. This potential problem can be alleviated by using a single wafer for each half by using laser etching for the necessary multiple depths [7].

7.0 Development of Power Combining THz multiplier

7.1 Introduction

Advances in power generating at THz frequencies continue to grow. THz multipliers at frequencies about 2 THz have been demonstrated [8-10]. While the fabrication of the active devices continues to improve, these very high frequency circuits have trouble achieving relatively high power levels due to understandably low efficiency levels. As the electronics continue to improve, higher power levels are achievable by using multiple active devices.

A popular option for generating higher power is simply to use multiple active devices on the same substrate, such as power amplifier applications. While this can be a good approach at low frequency, the losses associate with planar transmission lines (radiation, substrate, ohmic) at very high frequency make this approach less suitable.

Spatial or Quasi-optical combining is another attractive approach [11-13]. This technique has been demonstrated up to 450 GHz, but in sufficient power was available to saturate the circuits for a good conclusion. These system are also relatively bulky, thus would not be a good option for a compact design.

Since waveguide offers a confined low loss medium for signal conduction, we seek to utilize these properties for power combining similar to [14]. A waveguide approach offers a much simpler configuration than that of spatial combining.

7.2 Design

In this work, we utilize the Heterostructure-Barrier-Varactor (HBV) diode fabricated on an InP-based material [15]. Utilizing HBV diodes offers some advantages over Schottky diodes. Since HBV diodes only produce odd order harmonics, the design negates the need for an idler circuit. In addition, this HBV diode does not require bias, thus simplifying the block design as well. The HBV diode is flip-chip mounted on an AlN substrate. The input of the AlN circuit begins with a probe, which lies in the w-band input waveguide. This probe efficiently feeds the signal through a low pass filter before the HBV diode. The low pass filter will prevent the output signal from reaching the input waveguide. The output of the circuit also has a probe extending into a WR-3 waveguide to transition between the microstrip to waveguide. A photograph of the circuit mounted in a brass block is shown in Fig. 57.

For this design, it is necessary to split the input signal as well as recombine the output signal after multiplication. To accomplish this we elect to use the waveguide branch-line coupler. Using this coupler will allow us to better isolate diode circuits from each other. Extensive work has been performed on waveguide branch-line couplers [16].

For the input of the power combining circuit, a w-band 3dB waveguide coupler is needed to serve as the power splitter to feed each diode circuit. The requirements for this coupler are to split the power equally and to maintain a similar match to that of a single diode circuit block. The coupler is simulated and tuned in HFSS over an 85-92 GHz input frequency range. After the standalone coupler is optimized, the coupler is integrated with two input sections of the diode circuits as well as feeding networks to account for fabrication concerns (waveguide flanges, alignment pins, etc.). The layout of this simulation is shown in Fig 58. The match presented to the diode circuit from the W-band branch line coupler compared to that of a single diode is relatively good with the results shown in Fig. 59.

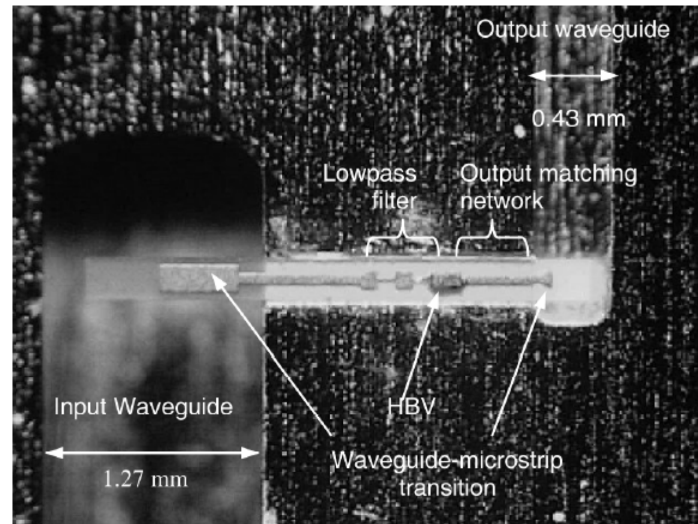

Fig. 57 The HBV diode mounted on an AlN substrate.

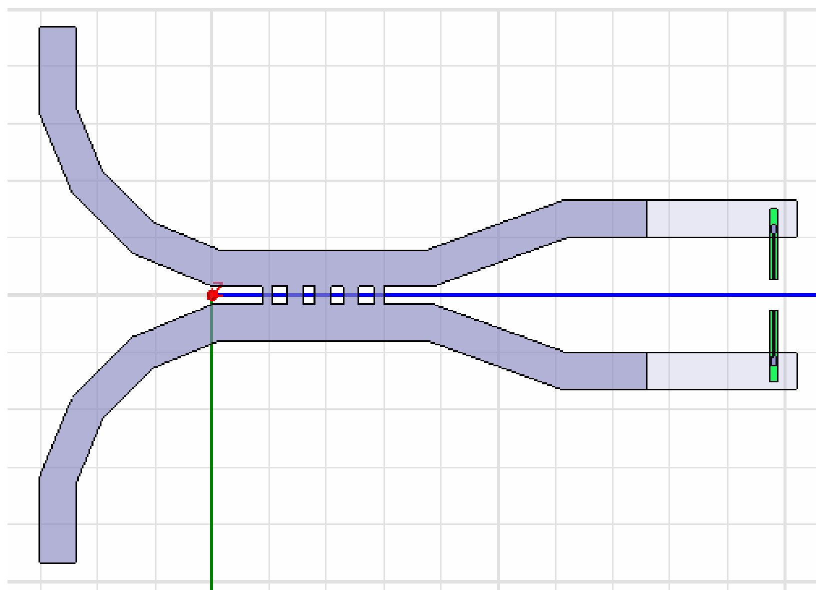

Fig. 58 Basic layout of the multiplier waveguide block.

The output coupler is to serve as the power combiner. This branch-line coupler is in waveguide size WR-3 and has requirements of providing a similar match to that of a single diode circuit block and efficiently combing the output power. The layout for this simulation is similar to that of the w-band coupler simulation. The results also showed a good agreement between the match presented to the diode from the WR-3 branch-line coupler as compared to that of a single diode circuit block. The match results are simulated from 255-276 GHz and are very good.

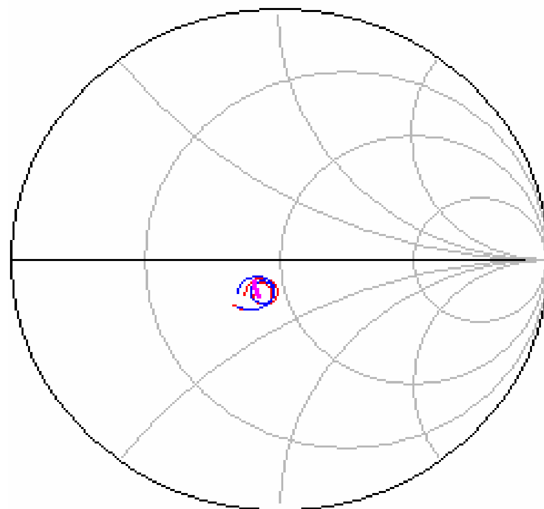

Fig. 59 Simulation results of the output combiner section versus and single output section from 255-276 GHz.

The composite assembly of the W-band branch line coupler, the diode channels and the WR-3 branch line coupler is shown in Fig. 60.

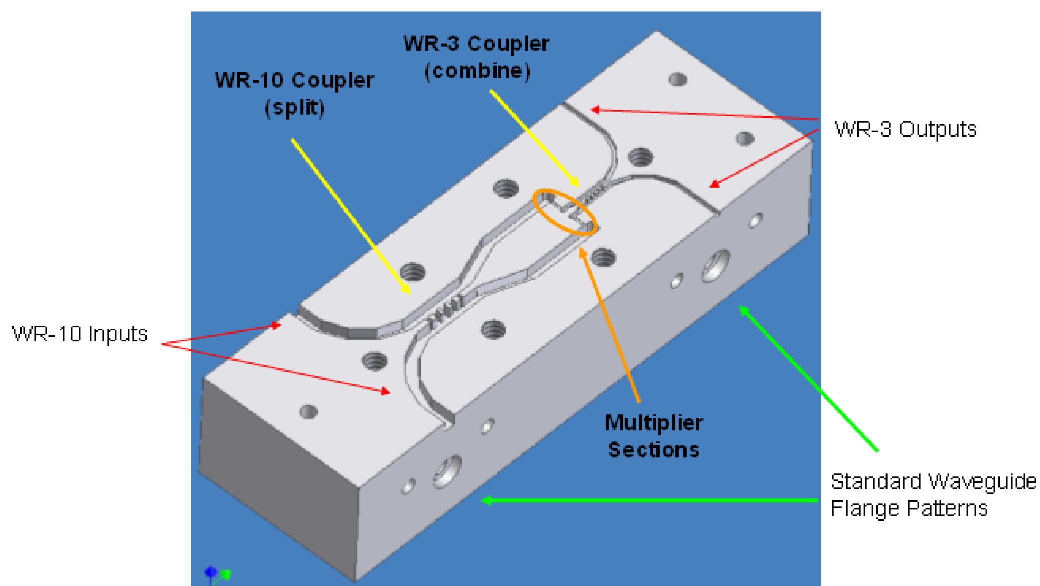

Fig. 60 Basic layout of the multiplier waveguide block.

7.3 Fabrication

While our previous work successfully utilized micromachined silicon waveguide to form the waveguide structures [17], our current micromachining technology does not allow for construction of the branch-line couplers with the needed multiple layers. While develop a more suitable design for silicon micromachining, we elect to fabricate this design in a brass block.

The bulk of the brass block was easily fashioned using standard milling techniques. The channels of the branch line couplers proved difficult for standard milling techniques. The small sections were formed using electrical discharged machining (EDM). EDM proved to be a very accurate technique, but should be noted is relatively expensive. A photograph of one-half of the fabricated block is shown in Fig. 61l. The diode circuits were installed into the combiner block using a UV-cured epoxy. A photograph of the installed diode circuits is shown in Fig. 61r.

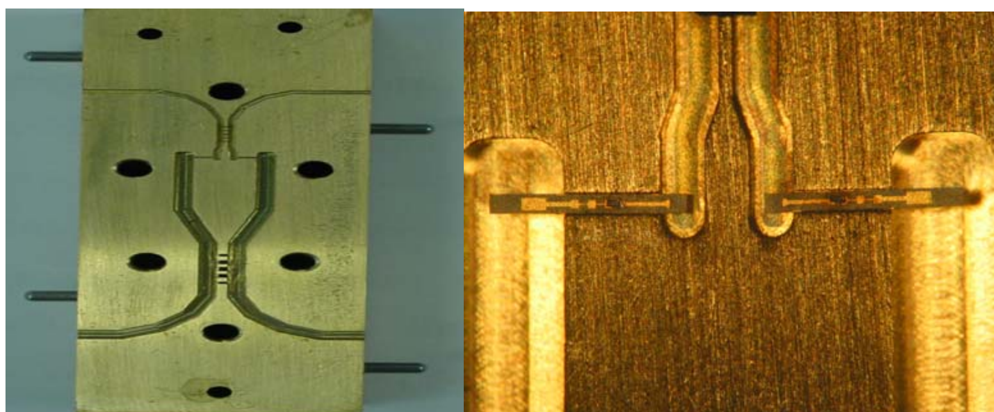

Fig. 61 (l) Photo of one-half of the fabricated block, and (r) “close-up” of the diode area.

7.4 Measurements

At the time of this measurement, high W-Band input power was not available. The combiner was characterized with maximum input power possible at each frequency. The W-Band signal was created by a multiplier chain, which begins with an Agilent E8247C Signal Generator. This generator provides a signal from 10.5 to 11.125 GHz.

This signal is fed into a Spacek Labs amplifier to provide a high drive level for the Spacek quadrupler. The frequency at this point is in the range of 42.0 to 44.67 GHz. The output of the quadrupler is WR-19 waveguide. This output is fed through a WR-19 waveguide variable attenuator. This attenuator will help control the input power level to the DUT.

The final multiplier is a D-90 doubler from Virginia Diodes, Inc. The input is WR-19 and the output is WR-10. An isolator is attached to the output of this doubler to maintain a good match. The output of the doubler is fed through an Erickson WR-10 low loss coupler. The through port of the coupler provides the w-band signal to the DUT. The reflected or reverse or port is connected to a diode detector which will be used to characterize the reflected power from the DUT and the forward port is used to determine the available input power to the DUT.

The final component of the measurement setup an Erickson power sensor attached to an Erickson Instruments Ltd. PM-1B Power meter. The input waveguide size of the power sensor is

WR-10. Since the output of the multiplier is WR-3, a WR-10 to WR-3 transition is used to minimize reflections. The measurement setup is depicted in block diagram form in Fig. 62.

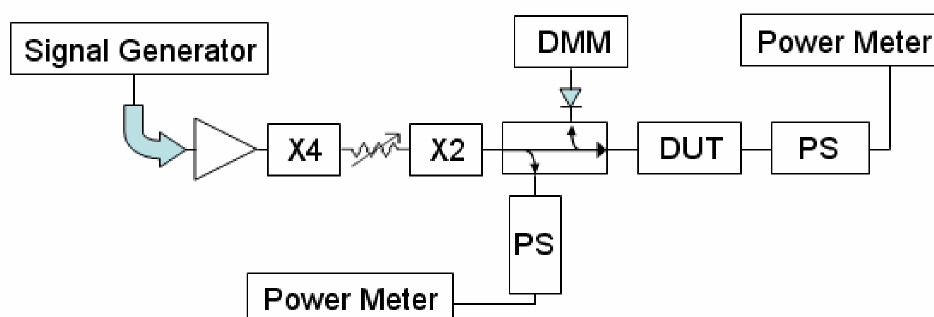

Fig. 62 Block diagram setup of the measurement setup.

The testing was performed with an input signal ranging from 84 GHz to 89 GHz. The input power available across this frequency range varied from 80 to 110 mW depending on the frequency. In an ideal case, the available power to each diode circuit would be half the total input power or 40 to 55 mW. This input power if far below what was needed to achieve both maximum input power and maximum efficiency of 110 mW [17].

For testing, the w-band isolated port at the input of the combiner block was terminated using a broadband w-band termination. Similarly, the isolated port of the WR-3 coupler was terminated with a WR-3 termination. The combiner block was tested at eleven frequency points, each of which was tested at nine different power levels. The maximum power level at each frequency point was tested and stepped down by 0.5dB until eleven points were measured. The output power versus input power of the combiner block is shown in Fig. 63.

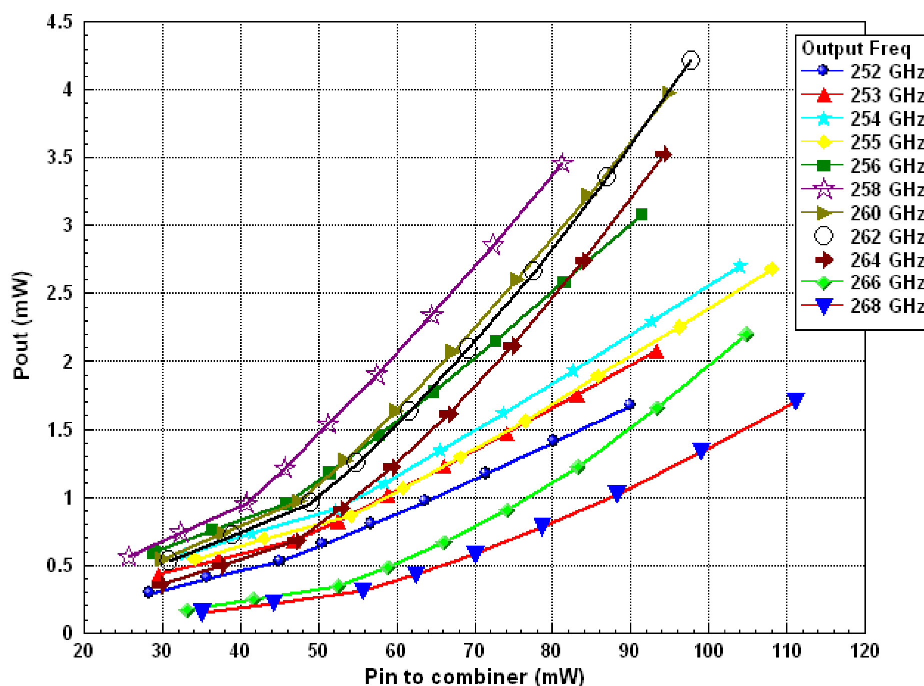

Fig. 63 Output power versus input power of the combiner block.

The results of the measurement show peak operation between 258-264 GHz, with the maximum output power at 262 GHz. For comparison purposes, a single diode circuit is evaluated at one-half the maximum input power to the combiner block. The output power of the single diode circuit is doubled, representing an ideal case of using two diode circuits. This doubled output power of a single diode circuit is compared to that of the combiner block at four frequency points in the table shown below. The difference represents how much less power the combiner circuit generates as compared to the ideal case.

Output Freq (GHz)	SM (mW)	SMx2 (mW)	Comb (mW)	Diff (dB)
256	1.79	3.58	3.08	-0.653
258	1.95	3.90	3.46	-0.520
260	2.19	4.38	3.98	-0.416
262	2.34	4.68	4.20	-0.470

Comparison of the combiner block versus a single diode performance at the same input power. SM=output power of a single diode, SMx2=double the input power of a single diode, Comb=output power of the combiner block and Diff=the difference between the output power of the combiner block and twice the output power of a single diode.

References

[1] P. L. Kirby, D. Pukala, H. Manohara, I. Mehdi, J. Papapolymerou, “Characterization of micromachined silicon rectangular waveguide at 400 GHz,” *IEEE Microwave and Wireless Components Letters*, pp. 366-368, June 2006.

[2] Y. Li, P. L. Kirby and J. Papapolymerou, “W-Band Folded and Straight Waveguide Using DRIE Technique,” *2006 IEEE International Microwave Symposium*, pp. 1915-1918, San Francisco, CA, June 2006.

[3] Y. Li, P. L. Kirby, J. Papapolymerou, "Silicon Micromachined W-Band Bandpass Filter Using DRIE Technique," 2006 European Microwave Conference, pp. 1271-1273.

[4] Q. Xiao, J. Hesler, T. Crowe, B. Deaver and R. Weikle II, “A 270 GHz Tuner-less Heterostructure Barrier Varactor Frequency Tripler,” *IEEE Microwave and Wireless Components Letters*, pp. ??? , ??? 2006.

[5] Q. Xiao, J. Hesler, T. Crowe, R. Weikle II, Y. Duan, and B. Deaver, “High Efficiency Heterostructure-Barrier-Varactor Triplers Using AIN Substrate,” *2005 IEEE MTT-S International Microwave Symposium Digest*, pp. 443-446, Long Beach, CA, June 2005.

[6] Q. Xiao, Y. Duan, J. L. Hesler, T. W. Crowe and R. Weikle II, “A 5-mW and 5% efficiency 210 GHz InP-based heterostructure barrier varactor quintupler,” *IEEE Microwave and Wireless Components Letters*, pp. 159-161, April 2004.

[7] C.K. Walker, G. Narayanan, H. Knoepfle, J. Capara, J. Glenn and A. Hungerford, “Laser Micromachining of Silicon: A New Technique for Fabricating High Quality Terahertz Waveguide Components,” *Proc. Eighth International Symposium on Space Terahertz Technology*, Harvard University, March 1997, pp. 358-376.

[8] T.W. Crowe, W.L. Bishop, D.W. Porterfield, J.L. Hesler and R.M. Weikle II, "Opening the terahertz window with integrated diode circuits," IEEE Journal of Solid-State Circuits, Oct. 2005 pp. 2104 - 2110.

[9] S. Martin, B. Nakamura, A. Fung, P Smith, J. Bruston, A. Maestrini, F. Maiwald, P. Siegel, E. Schlecht and I. Mehdi, "Fabrication of 200 to 2700 GHz multiplier devices using GaAs and metal membranes," 2001 IEEE MTT-S International Microwave Symposium Digest, May 2001, pp. 1641 - 1644.

[10] F. Maiwald, S. Martin, J. Bruston, A. Maestrini, T. Crawford and P. Siegel,"2.7 THz waveguide tripler using monolithic membrane diodes," 2001 IEEE MTT-S International Microwave Symposium Digest, May 2001, pp. 1637 - 1640.

[11] B. Schumann, M. Hoft and R. Judaschke, "A multi-element 150/300 GHz spatial power dividing/combining frequency doubler," 2002 IEEE MTT-S International Microwave Symposium Digest, June 2002, pp. 1539 - 1542.

[12] B. Schumann, M. Hoft, M. Saglam, H.L. Hartnagel and R. Judaschke, "A 5 element 450 GHz HBV frequency tripler," 2003 IEEE MTT-S International Microwave Symposium Digest, June 2003, pp. 759 - 762.

[13] R. Judaschke, M. Hoft and K. Schunemann, "Quasi-optical 150-GHz power combining oscillator," IEEE Microwave and Wireless Components Letters, May 2005, pp. 300 - 302.

[14] A. Maestrini, C. Tripon-Canseliet, J.S. Ward, J.J. Gill and I. Mehdi, "A 260-340 GHz Dual Chip Frequency Tripler for THz Frequency Multiplier Chains," Joint 31st International Conference on Infrared Millimeter Waves and 14th International Conference on Teraherz Electronics, Sept. 2006, pp. 336 - 336.

[15] Q. Xiao, J.L. Hesler, T.W. Crowe, B.S. Deaver and R.M. Weikle, "A 270-GHz Tuner-Less Heterostructure Barrier Varactor Frequency Tripler," IEEE Microwave and Wireless Components Letters, April 2007, pp. 241 - 243.

[16] H. Andoh, T. Minamidani, S. Asayama, Y. Yonekura and H. Ogawa, “Designs of Wideband 3dB Branch-line Couplers for ALMA Band 3 to 10,” ALMA Memo 468, www.alma.nrao.edu.

[17] P.L. Kirby, Y. Li, Q. Xiao, J.L. Hesler and J. Papapolymerou, "Silicon Micromachined Multiplier Utilizing Heterostructure Barrier Varactor Diode," 2007 IEEE MTT-S International Microwave Symposium, 2007, June 2007, pp. 1141 - 1144.